Efficient Sensor Array Subsampling for Plane-Wave Ultrasound Imaging

by

Houssem Marzougui
BSc, United States Naval Academy, 2011

A Thesis Submitted in Partial Fulfillment
of the Requirements for the Degree of

MASTER OF APPLIED SCIENCE

in the Department of Electrical and Computer Engineering

University of Victoria

Supervisory Committee

Efficient Sensor Array Subsampling for

Plane-Wave Ultrasound Imaging

by

Houssem Marzougui
BSc, United States Naval Academy, 2011

Supervisory Committee

Dr. Daler Rakhmatov, Department of Electrical and Computer Engineering

Supervisor

Dr. Mihai Sima, Department of Electrical and Computer Engineering

Departmental Member

Abstract

Supervisory Committee

Dr. Daler Rakhmatov, Department of Electrical and Computer Engineering

Supervisor

Dr. Mihai Sima, Department of Electrical and Computer Engineering

Departmental Member

Ultrafast plane-wave ultrasound imaging offers very high frame rates (exceeding thousands of frames per second) but entails large volumes of backscattered data collected by a sensor array over multiple plane-wave emissions at different angles. We propose a simple method for reducing the total amount of sampled data. First, we acquire the zero-angle data in full, and then we perform deterministic subsampling of the remaining nonzero-angle data. Our subsampling patterns are angle-specific and derived based on the zero-angle data using a Fourier-domain migration technique. We use two experimental datasets to evaluate the benefits and drawbacks of our proposed method in terms of spatial resolution and contrast-to-noise ratio, observed in the resulting B-mode images.

Table of Contents

List of Tables

List of Figures

Acknowledgements

First and foremost, I would like to express my most sincere gratitude to my supervisor Dr. Daler Rakhmatov for his encouragement, support and guidance throughout the course of my Master's program. Further, I thank Dr. Mihai Sima (my supervisory committee member) for his help with examining my thesis.

Dedication

To My Parents (Mohamed Mahjoub Marzougui and Bellara Ayachi), To My Sisters Abir and Nihel

For their endless love, support and encouragement

List of Acronyms

Plane Wave	PW
Coherent Plane-Wave Compounding	CPWC
Compressive Sensing	CS
Contrast-to-Noise Ratio	CNR
Delay-and-Sum [Beamforming]	DAS
Full Acquisition	FA
Full Width at Half Maximum	FWHM
Computed Tomography	CT
Radio Frequency	RF
Time Gain Compensation	TGC
Analog-To-Digital Converter	ADC
Region of Interest	ROI
Steered Plane Wave	SPW
Exploding Reflector Model	ERM

Ultrasound Fourier-Slice Beamforming	UFSB
Finite Rate of Innovation	FRI
Alternating Direction Method of Multipliers	ADMM
Non-Uniform Fourier Transform	NUFT
Point Spread Functions	PSF
Inverse Problem	IP

Chapter 1: Introduction

1.1 Ultrasound Imaging Principles

Ultrasound imaging is a widely used technique in producing images of the interior of the human body using sound waves. In the late 1970s, the first ultrasound system was built and used for real time medical imaging [1]. A study showed that in 2011 alone, more than 2800 million medical ultrasound imaging procedures were performed per year, compared to only 160 million procedures for Computed Tomography (CT) and 80 million procedures for Magnetic Resonance Imaging (MRI) [54]. This continuous immense interest in ultrasound is mainly credited to its low cost, no ionizing radiation effects, non-invasive nature, fast (even ultra-fast) data acquisition and processing, and ease of access (mobile and miniaturized scanners).

Ultrasound imaging is based on the physical principle of echography, where an interaction of acoustic waves with an insonified medium (such as living tissues) occurs, to create dynamic and real-time images that can be analyzed to obtain quantitative structural and functional information from imaged body sections [2]. These acoustic waves are in fact mechanical waves characterized by fluctuations of pressure and density, which cause particles displacements around their equilibrium state. These waves are described by the following equation in a homogenous medium [27]:

$$\left[\Delta - \frac{1}{c^2}\frac{\partial^2}{\partial t^2}\right] p(\vec{r}, t) = 0, \qquad (1.1)$$

where p is the wave pressure as a function of space and time t, Δ is the Laplace operator, and c is the wave propagation speed.

There are several imaging modes, or techniques, available to produce an image that captures the interactions between the sound waves and the living tissues [2]. The most common techniques are listed below:

- Amplitude mode, or A-mode, is the simplest ultrasound technique, whereby a transducer scans a single line through the medium, with the backscattered signals plotted as a one-dimensional function of depth [64].
- Brightness mode, or B-mode, involves a transducer scanning multiple adjacent lines through the medium, which can then be displayed as a two-dimensional grayscale image, where the pixel brightness indicates the echo signal intensity [64].
- Motion mode, or M-mode, entails a rapid sequence of B-mode scans to measure and display a range of motions, as organ reflections move relative to the transducer [64].
- Doppler mode relies on the Doppler effect to determine and visualize blood flow velocity and direction [64].

This thesis focuses on the B-mode, also known as 2D real-time imaging, since it produces a 2D gray-scaled image of the tissues in real-time.

Ultrasound systems use various transducers to send the sound waves into the human body and to receive the backscattered signals for acquisition and processing. In general, most diagnostic and intravascular transducers use

frequencies that range between 3 MHz and 30 MHz [3], even up to 100 MHz for ultrasound bio-microscopy systems [4] [5]. The propagation velocity of these sound waves is assumed constant in human soft tissues and equal to 1540 meters per second [6]. As a result, the acoustic impedance is only evaluated as a function of tissue density [2]. A greater density of the tissue leads to stronger backscattered signals received by the transducer, and the brighter corresponding areas in the final image.

1.2 Typical Ultrasound System

Figure 1.1 shows a typical ultrasound system. The key component of this system is the transducer, also known as a probe, that has two modes of activation: sending and receiving. It consists of a series of piezo-electric transducer elements (usually between 64 and 256 elements) that convert electrical energy into sound wave energy and vice versa [14]. Collectively, they are able to emit a focused beam wave, a plane wave (PW), or a divergent wave into the living tissue. In the case of PW, the width b of each of the piezo-electric elements needs to be:

$$b = \frac{\lambda}{2}, \qquad (1.2)$$

where λ is the wavelength of the emitted sound signal. This width guarantees the emittance of a circular wave from each piezo-electric element due to diffraction. Combined together, these circular waves would form a plane wave traveling into the medium. If b is greater than λ, the diffraction effect decreases and the formation of a plane wave fails.

The distance d between neighboring piezo-electric elements (also known as pitch) should be:

$$d = \frac{\lambda}{2}. \qquad (1.3)$$

The piezo-electric elements at the extremity of the transducer have no neighbors, which would cause side lobes artifacts. An apodization solution is implemented to remove these lobes, but it leads to some power loss at the extremities of the probe. One may also observe grating lobes caused by constructive interferences appearing outside of the focal region, and usually (when we have a pitch > λ) they would reduce image quality [8]. One of the most challenging and interesting phenomena in ultrasound imaging is the scattering effect due to structures with dimensions smaller than λ (such as blood red cells), also known as the speckle phenomenon [16].

In the receiving mode, a backscattered analog radio frequency (RF) signal is amplified when it goes through a time gain compensation (TGC) to compensate the absorption effect that attenuates the emitted signal's energy level [8]. Once amplified, the analog RF signal is then converted into the digital RF signal using an analog-to-digital converter (ADC) to allow for signal processing phase. A Beamformer control unit receives the digitized raw RF channel data and performs image reconstruction, followed by envelope detection to extract the envelope of the beamformed data. To change the dynamic range of the resulting envelope, logarithmic compression is typically performed to adjust the image for final display [10].

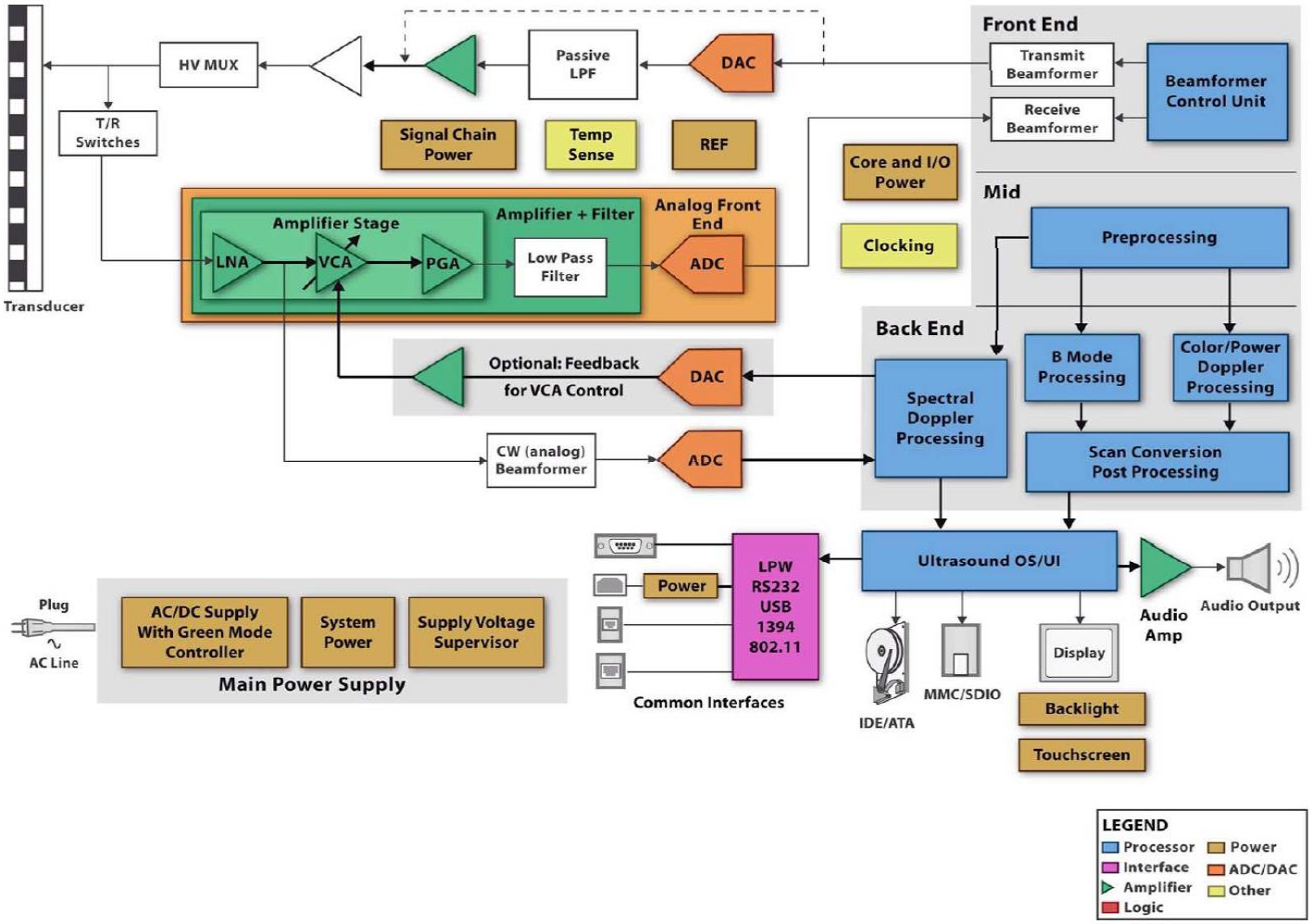

Figure 1.1: Ultrasound system components [7]

1.3 Ultrasound Image Quality

Several parameters convey the quality level of ultrasound imaging, such as the spatial resolution, the contrast, and the frame rate.

1.3.1 Spatial Resolution

In ultrasound imaging, spatial resolution allows us to differentiate between two points at a particular position in a living tissue that we are trying to diagnose [12]. Figure 1.2 shows two main components of spatial resolution: axial and lateral.

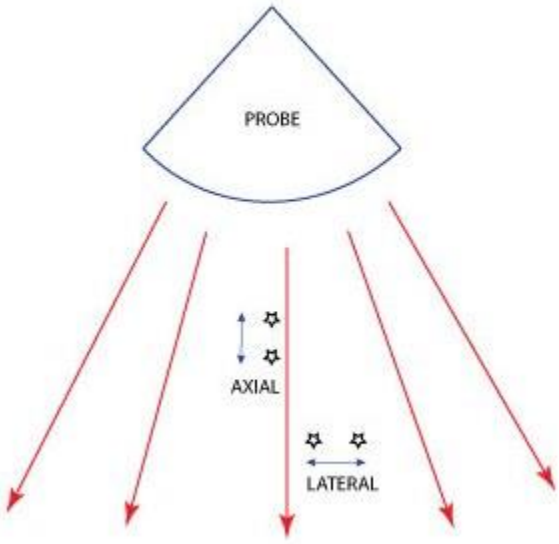

Figure 1.2: Spatial resolution: Axial + Lateral in ultrasound imaging [13]

Axial resolution, also known as longitudinal resolution, is the minimum distance between two reflectors that are located in the direction of an ultrasound beam [12]. Axial resolution can be expressed as follows:

$$R_{Axial} = \frac{cN}{2f_0} = \frac{\lambda N}{2}, \qquad (1.4)$$

where c is the speed of sound in a soft tissue, f_0 is the transmitted pulse frequency (operating frequency of the transducer), λ is the pulse wavelength, and N is the number of cycles in the transmitted pulse. To account for pulse roundtrip delay in the medium (from emission to reception) the axial resolution is divided by a factor of 2. We can also observe that higher frequency pulses imply higher axial resolutions, but at high frequencies, the maximum depth decreases, and attenuation effects become more severe (i.e., the energy of the backscattered pulses become weaker for the transducer detection [12]).

Lateral resolution, as opposed to the axial resolution, is the minimum distance between two reflectors placed perpendicularly to the ultrasound beam direction [12]. It can be expressed as follows [15]:

$$R_{Lateral} = \frac{\lambda z}{b} = \lambda F\#\,, \qquad (1.5)$$

where λ is the pulse wavelength, z is the depth of the target object or structure, b is the width of the active piezo-electric elements, and $F\#$ is the so-called F-number of the imaging system.

1.3.2 Contrast

The contrast quality refers to how well a region of interest (ROI) appears with respect to its background. Specifically, the contrast-to-noise ratio (CNR) can be expressed as follows [17]:

$$CNR = 20log_{10}\left(\frac{|\mu_{in} - \mu_{out}|}{\sqrt{\frac{(\sigma_{in}^2 - \sigma_{out}^2)}{2}}}\right), \quad (1.6)$$

where μ_{in} is the average signal level inside the ROI, μ_{out} is the average signal level in the surrounding background, σ_{in} and σ_{out} are the standard deviations inside and outside the ROI. The contrast reduces in value in the presence of side lobes and grating lobes.

1.3.3 Frame Rate

In conventional ultrasound imaging, the frame rate is given by:

$$F_{rate} = \frac{c}{2zN_{lines}}\ , \quad (1.7)$$

where c is the speed of sound in a soft tissue, z is the depth of the imaged section, and N_{lines} is the number of scan lines. For example, for a scan of 128 lines reaching 5 cm depth, $F_{rate} = 120\ fps$. Ultrafast imaging can yield a much higher frame rate due to its steered plane wave (SPW) technique:

$$F_{rate} = \frac{c}{2zN_{spw}}\ , \quad (1.8)$$

where N_{spw} is the number of steered plane waves emitted. For example, using $N_{spw} = 5$ and $z = 5\ cm$, we would get $F_{rate} = 3080\ fps$. Increasing the number of plane waves N_{spw} considerably improves the image quality, but reduces the resulting frame rate.

1.4 Ultrasound Plane-Wave Imaging

As mentioned above, plane wave imaging allows for very high frame rates [11]. Figure 1.3 shows an example of a steered plane wave emitted into the insonified medium at an angle θ. These steered plane waves are generated by applying appropriate transmit delays to individual piezo-electric transducer elements, similar to the way phased arrays operate [62].

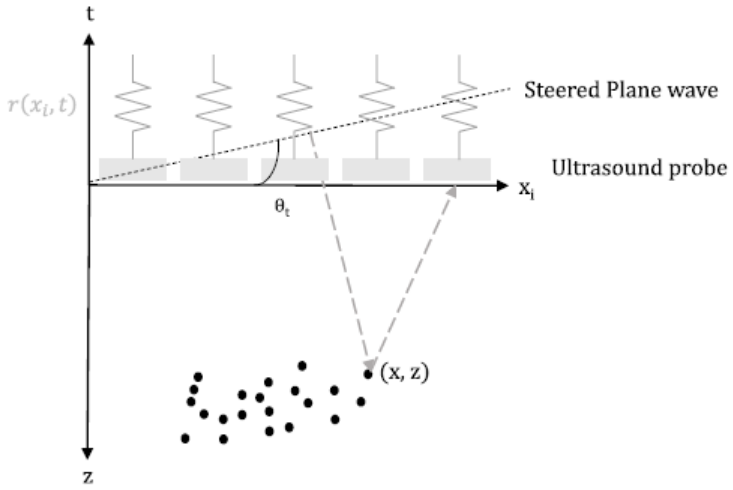

Figure 1.3: Steered plane wave [36]

A conventional method to perform plane-wave image reconstruction is to apply a non-adaptive delay-and-sum (DAS) beamformer in the time domain as shown in Figure 1.4. Generally, a DAS beamformer exploits the concept of time delays to focus the backscattered echoes. Figure 1.5 (a) shows the distance a signal travels to and from a point located at (x, z) in the medium to a sensor positioned at x_1. Each point (x, z) of the image is obtained by adding coherently the contribution of each scatter, i.e., delaying the $RF(x_1, t)$ signals by $\tau(x_1, x, z)$ and adding them together over all sensor positions. Thus,

we obtain the beamformed data point $BF(x,z)$ from raw RF data as follows:

$$BF(x,z) = \sum_{all\ x_1} RF(x_1, \tau(x_1,x,z)). \quad (1.9)$$

Figure 1.5 (a) is the case of sending a plane wave with a zero angle. Figure 1.5 (b) shows the distance these echoes travel in the case of an SPW having an angle θ. Montaldo *et al.* [19] showed that based on the axial coordinate equation of $z = ct/2$, we can obtain the time delay as:

$$\tau(\theta, x_1, x, z) = \tau_{tx}(\theta, x, z) + \tau_{rx}(x_1, x, z) = \frac{\left(z\cos(\theta) + x\sin(\theta) + \sqrt{z^2 + (x_1 - x)^2}\right)}{c}, \quad (1.10)$$

where $\tau_{tx}(\theta, x, z) = z\cos(\theta) + x\sin(\theta)$ is the delay the transmitted sound wave takes to travel from the transducer array to point (x,z) and $\tau_{rx}(x_1, x, z) = \sqrt{z^2 + (x_1 - x)^2}$ is the delay that a reflected echo takes to travel back to a sensor located at x_1.

According to [19], using plane waves may yield lower image quality because the beamforming process is restricted to the receive mode, i.e. there is no transmit focusing. To overcome this problem, we need to use multiple steered plane waves, resulting in multiple angle-specific beamformed frames Given a set of N plane waves with steering angles $\theta_i, i = 1, \dots, N$, we apply DAS beamforming N times. The resulting N beamformed frames are then added coherently to obtain a final compounded image [19]. Such coherent plane-wave compounding (CPWC) is executed before applying the envelope detection and logarithmic compression, whereas so-called incoherent plane-wave compounding is applied

to the enveloped-detected images (to reduce speckle noise and increase signal to noise ratio) [19]. Figure 1.6 shows how CPWC is applied by adding three different beamformed frames to obtain a single compounded frame.

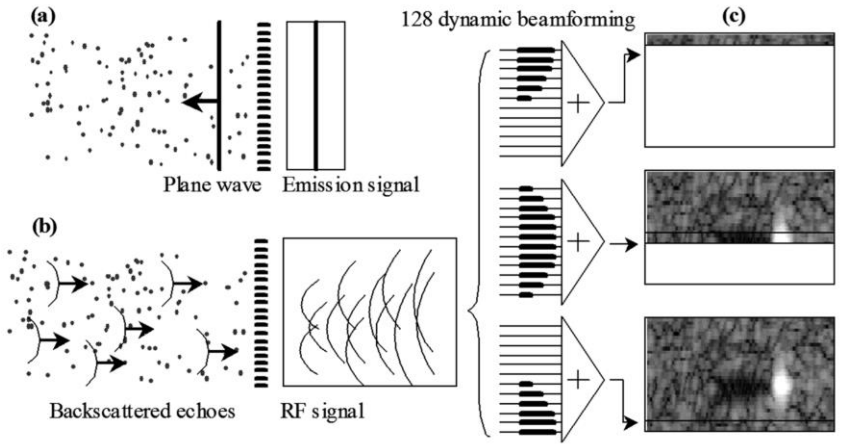

Figure 1.4: Delay-and-Sum (DAS) beamformer, (a) Medium insonification with a plane wave transmission, (b) Backscattered RF signals recording, (c) Beamforming by applying time delays and signals summation [19].

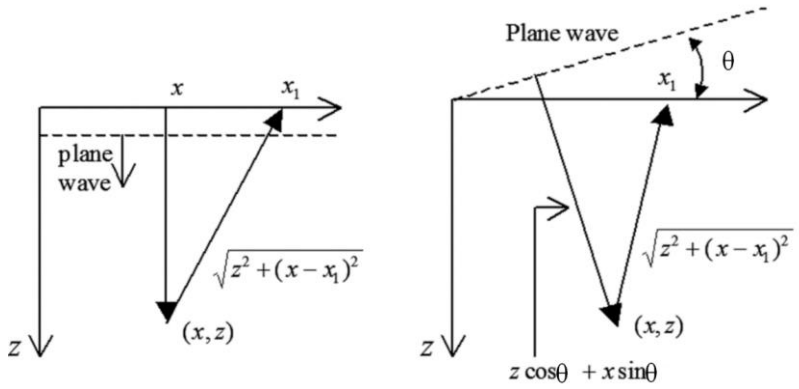

(a) (b)

Figure 1.5: (a) Time delays for a plane wave insonification, (b) Time delays for a plane wave steered at an angle θ [19].

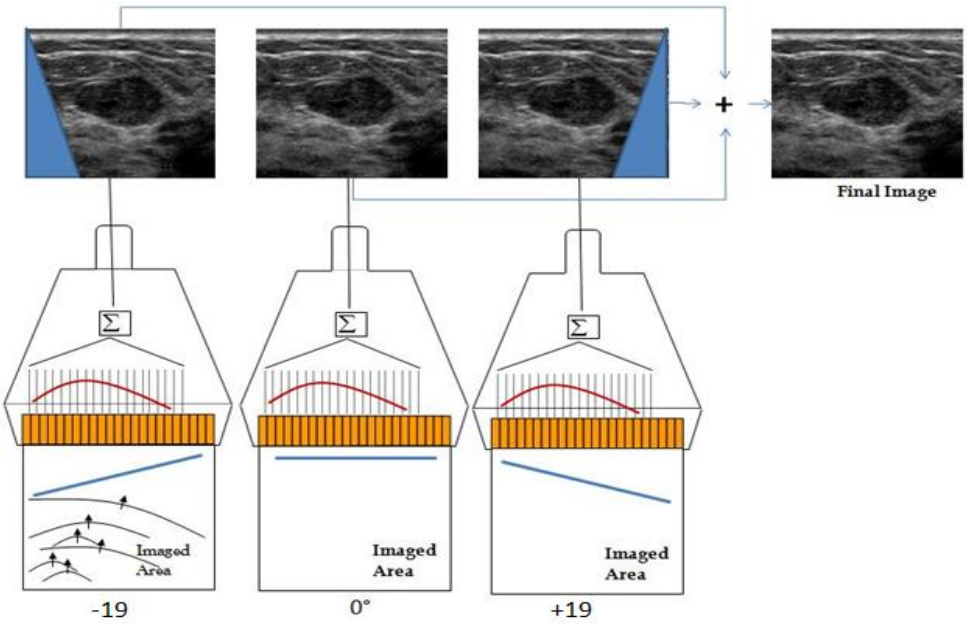

Figure 1.6: Coherent Plane-Wave Compounding (CPWC) [19], [63].

In this work, we perform plane-wave image reconstruction in the Fourier domain using modified Stolt's migration method from [30]. Its use is motivated by the fact that its computation cost is substantially lower compared to conventional DAS beamforming [30], [55]. Further details on modified Stolt's migration technique are provided in chapter 2.

1.5 Thesis Contribution

Our goal is to explore the possibility of considerable raw RF data savings during CPWC data acquisition, while preserving an acceptable image quality. We propose to initially perform a full acquisition of the zero-angle data, and then apply deterministic subsampling of the remaining nonzero-angle data. Our novel subsampling scheme identifies sensor array sampling patterns, which are angle-specific and based on applying modified Stolt's migration in reverse. We also

explore several options of improving the resulting image quality to mitigate the negative effects of subsampling.

The rest of the thesis is organized as follows. In chapter 2, we will discuss different frequency-domain image reconstruction and data reduction techniques, highlighting modified Stolt's migration technique used in this work. In chapter 3, we will introduce our proposed subsampling scheme and possible ways to enhance the final image quality. In chapter 4, we will discuss subsampled experimental imaging results evaluated in terms of resolution and contrast. Finally, in chapter 5, we will draw our conclusion and outline possible directions for future work.

Chapter 2: Background

2.1 Fourier Methods for Image Reconstruction:

This thesis deals with two major approaches used for image reconstruction. First is nonadaptive delay-and-sum (DAS) beamforming (described in chapter 1), applied to backscattered echoes sequentially per scanline in the time domain [19], [20] or the temporal frequency domain [31]. Second is a Fourier-domain approach described next [21], [22], [23], [24]. We begin by forming the 2D Fourier spectrum of the raw RF data. The (k_x, f)-domain data (where f represents the temporal frequencies and k_x the spatial frequencies) are then remapped using certain coordinate transformations into the (k_x, k_z)-domain data, where k_z represents the spatial frequencies related to the z-axis of the reconstructed image in the (x, z)-domain [30]. Finally, the remapped spectrum undergoes an inverse Fourier-transform to obtain the 2D final image data points in the (x, z)-domain.

The Fourier-domain techniques reported in the ultrasound literature are: Lu's method [22], ultrasound Fourier-Slice Beamforming (UFSB) [21], [24], Garcia's method [23], and the modified Stolt's method [30]. Lu's method [22] is based on the theory of limited-diffraction beams [44], and it remaps data points from the (k_x, k)-domain to the (k_x, k_z)-domain based on the following equation [22]:

$$\left(k_x, \frac{{k_x}^2 + {k_z}^2}{2k_x \sin(\theta) + 2k_z \cos(\theta)}\right), \tag{2.1}$$

where θ is the steering angle of an emitted plane wave, and $k = f/c$. The Fourier-Slice beamforming method [21] is based on the Fourier Slice theorem [24], and it implements the following remapping formula:

$$\left(\frac{{k_x}^2 + {k_z}^2}{2k_x \sin(\theta) + 2k_z \cos(\theta)}, arctan\left(\frac{2k_x\, k_z \cos(\theta) + ({k_x}^2 - {k_z}^2)\sin(\theta)}{2k_x k_z \sin(\theta) + ({k_z}^2 - {k_x}^2)\cos(\theta)} \right) \right), \qquad (2.2)$$

using polar coordinates (k_x, α), where $\sin(\alpha) = k_x/k$. Garcia's method [23] is based on the $f-k$ (frequency - wavenumber) seismic migration under the exploding-reflector model (ERM) assumptions [25]:

$$\left(k_x, \frac{\sqrt{{k_x}^2 + {k_z}^2 S^2}}{\sqrt{1 + \cos(\theta) + sin^2(\theta)}} \right), \qquad (2.3)$$

where $S = (1 + \cos(\theta) + sin^2(\theta)/(1 + \cos(\theta))^{1.5}$. Note that before remapping using (2.3), the k_x-axis data locations are shifted by $-ksin\theta$ (the same shift is applied in Lu's method).

Modified Stolt's method [30] is also based on the ERM assumptions, but it differs from Garcia's method in that it uses appropriate adjustments of reflector explosion times rather than fitting ERM-based travel time hyperbolas [23], [30]. Since this method is the one we adapted in this thesis, its technical details are presented next, borrowed from [30].

2.1.1 Classic Stolt's Migration

Stolt's method is one of the fastest techniques in the (f, k_x)-domain [26]. It is based on the exploding reflector model (ERM) [23] where we assume that all reflectors in the medium explode simultaneously at *t* = 0 (Figure 2.1).

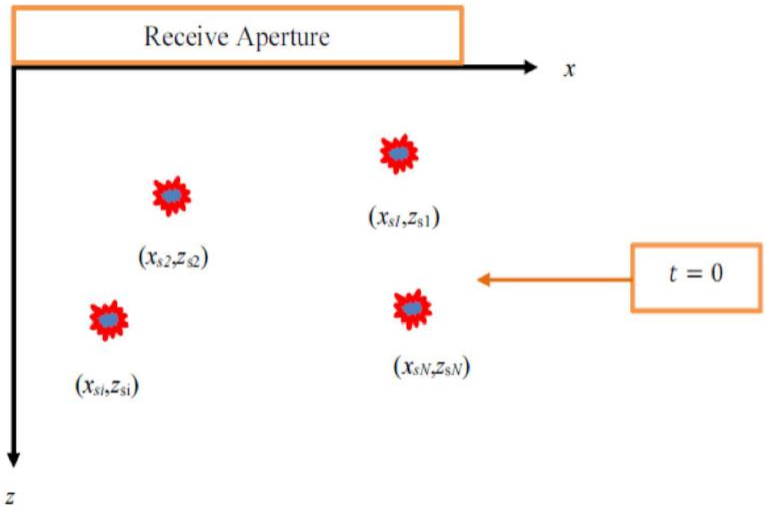

Figure 2.1: Exploding Reflector Model (ERM) [25].

To understand the original algorithm, we first rewrite equation (1.1) as follows:

$$\left[\Delta - \frac{1}{v^2}\frac{\partial^2}{\partial t^2}\right] P(x,z,t) = 0, \qquad (2.4)$$

where $v = \frac{c}{2}$ is the one-way propagation velocity (from the exploding reflector to the receiving sensors) according to the ERM model. The wave pressure is given by:

$$P(x,z,t) = \iint \Psi(k_x,z,f) e^{j2\pi(k_x x + f.t)}\, dk_x df, \qquad (2.5)$$

where $\Psi(k_x,z,f)$ is the 2D Fourier transform of $P(x,z,t)$, k_x is the spatial frequency, and f is the temporal frequency. From equations (2.4) and (2.5), we obtain:

$$\iint \left[\frac{\partial^2}{\partial t^2} + \left(\frac{4\pi^2 f^2}{v^2} - 4\pi^2 k_x^2\right)\right] \Psi(k_x,z,f) e^{j2\pi(k_x x + ft)}\, dk_x df = 0. \qquad (2.6)$$

Letting $k_z^2 = \frac{f^2}{v^2} - k_x^2$, equation (2.6) becomes:

$$\iint \left[\frac{\partial^2}{\partial t^2} + (4\pi^2 k_z^2)\right] \Psi(k_x, z, f) e^{j2\pi(k_x x + ft)}\, dk_x df = 0. \qquad (2.7)$$

Since equation (2.6) is equal to zero, we have:

$$\left[\frac{\partial^2}{\partial t^2} + (4\pi^2 k_z^2)\right] \Psi(k_x, z, f) = 0. \qquad (2.8)$$

The general solution of equation (2.7) is given by:

$$\Psi(k_x, z, f) = \quad C_{down}(k_x, f) e^{-j2\pi k_z z} + \; C_{up}(k_x, f) e^{-j2\pi k_z z}, \qquad (2.9)$$

where $C_{down}(k_x, f)$ and $C_{up}(k_x, f)$ are the solutions for the downgoing and upgoing waves. However, our ERM model only focuses on the $C_{up}(k_x, f)$ part and assumes $C_{down}(k_x, f) = 0$. Since the $C_{up}(k_x, f) = \Psi(k_x, z = 0, f)$, we get:

$$\Psi(k_x, z, f) = \quad \Psi(k_x, 0, f) e^{-j2\pi k_z z}. \qquad (2.10)$$

The above equation shows that it is possible to obtain the full 2D Fourier spectrum using an extrapolation operator $e^{-j2\pi k_z z}$ to extrapolate the $\Psi(k_x, 0, f)$ field to all $z > 0$ [28], [29]. Combining equations (2.5) and (2.10) at $t = 0$ (time of explosion) yields:

$$P(x, z, 0) = \iint \Psi(k_x, z = 0, f) e^{j2\pi(k_x x + k_z z)}\, dk_x df. \qquad (2.11)$$

Given that $k_z^2 = \frac{f^2}{v^2} - k_x^2$, we have $f = v k_z \sqrt{1 + \left(\frac{k_x}{k_z}\right)^2}$ and $df = \frac{v}{\sqrt{1+\left(\frac{k_x}{k_z}\right)^2}} dk_z$. Hence,

$$P(x,z,0)=\iint \frac{v\Psi\left(k_x,0,vk_z\sqrt{1+\left(\frac{k_x}{k_z}\right)^2}\right)}{\sqrt{1+\left(\frac{k_x}{k_z}\right)^2}}e^{j2\pi(k_xx+k_zz)}\,dk_xdk_z. \qquad (2.12)$$

2.1.2 Plane Wave Stolt's Migration

In ultrafast plane wave imaging, to apply Stolt's migration technique, we need to account for all the steered plane wave angles. First, we will discuss the case of the zero angle [30]. We begin by setting $v=c$ and multiplying $\Psi(k_x,0,f)$ by $e^{j2\pi f\frac{z}{c}}$ to compensate for over-migration of the positions of the reflectors along the z-axis. That is,

$$P(x,z,0)=\iint \Psi(k_x,z=0,f)e^{j2\pi\left(k_xx+k_zz+f\frac{z}{c}\right)}\,dk_xdf. \qquad (2.13)$$

To reduce equation complexity, we introduce a new parameter $\hat{k}_z$ [30] such that

$$\hat{k}_z=\frac{f}{c}+k_z=\frac{f}{c}\left[1+\sqrt{1-\left(\frac{ck_x}{f}\right)^2}\right], \qquad (2.14)$$

subject to $f^2>\ c^2k_x^2$, which implies $\hat{k}_z{}^2>\ k_x^2$. Now equation (2.13) becomes:

$$P(x,z,0)=\iint \Psi(k_x,z=0,f)e^{j2\pi\left(k_xx+\hat{k}_zz\right)}\,dk_xdf \qquad (2.15)$$

Since

$$f=\frac{c\hat{k}_z}{2}\left[1+\left(\frac{k_x}{\hat{k}_z}\right)^2\right]\Rightarrow\ \frac{df}{d\hat{k}_z}=\frac{c}{2}\left[1-\left(\frac{k_x}{\hat{k}_z}\right)^2\right], \qquad (2.16)$$

we obtain

$$P(x,z,0) = \iint \frac{c}{2}\left[1-\left(\frac{k_x}{\hat{k}_z}\right)^2\right]\Psi\left(k_x, z=0, \frac{c\hat{k}_z}{2}\left[1+\left(\frac{k_x}{\hat{k}_z}\right)^2\right]\right) e^{j2\pi(k_x x+\hat{k}_z z)}\, dk_x d\hat{k}_z. \quad (2.17)$$

We interpolate the f-axis to get the spectrum $\widehat{\Psi}(k_x, 0, \hat{k}_z)$ for $\hat{k}_z{}^2 > k_x^2$ (for values $\hat{k}_z{}^2 \leq k_x^2$, we set $\widehat{\Psi}(k_x, 0, \hat{k}_z) = 0$):

$$\widehat{\Psi}(k_x, 0, \hat{k}_z) = \frac{c}{2}\left[1-\left(\frac{k_x}{\hat{k}_z}\right)^2\right]\Psi\left(k_x, z=0, \frac{c\hat{k}_z}{2}\left[1+\left(\frac{k_x}{\hat{k}_z}\right)^2\right]\right). \quad (2.18)$$

For plane waves with angles other than zero, we need to transform the original z-axis into a new $\hat{z}$-axis. To get the new axis, we set:

$$\hat{z} = z^* + x\frac{tan\theta}{2}, \text{where } z^* = z\frac{1+cos\theta}{2}. \quad (2.19)$$

To incorporate the $\hat{z}$ transformation into equation (2.18), we use the scaling property of the Fourier transform:

$$\widehat{\Psi}_\theta(k_x, 0, \hat{k}_z) = \frac{c}{1+cos\theta}\left[1-\left(\frac{k_x}{\hat{k}_z}\right)^2\right]\Psi\left(k_x, z=0, \frac{c\hat{k}_z}{1+cos\theta}\left[1+\left(\frac{k_x}{\hat{k}_z}\right)^2\right]\right). \quad (2.20)$$

To obtain the (x,z)-domain image, we apply a 2D inverse Fourier transform $\widehat{\Psi}_\theta(k_x, 0, \hat{k}_z)$ to get $P_\theta(x, z^*, \theta)$, and then we interpolate along the z^*-axis using equation $\hat{z} = z^* + x\frac{tan\theta}{2}$ to obtain the final $P_\theta(x, \hat{z}, 0)$ that corresponds to our final image. In summary, the modified Stolt's method follows the steps outlined below [30].

Step 1: Obtain $\Psi(k_x, 0, f)$ by taking the Fourier transform of $P(x,t,0)$. For $f^2 \leq c^2k_x^2$, let $\Psi(k_x, 0, f) = 0$.

Step 2: Interpolate $\Psi(k_x, 0, f)$ along f-axis and scale the amplitude to get $\widehat{\Psi}_\theta(k_x, 0, \hat{k}_z)$. For $\hat{k}_z{}^2 \leq k_x^2$, let $\widehat{\Psi}_\theta(k_x, 0, \hat{k}_z) = 0$.

Step 3: Along the k_x-axis, apply the inverse Fourier transform to $\widehat{\Psi}_\theta(k_x, 0, \hat{k}_z)$ to get $P_\theta(x, z^*, 0)$.

Step 4: Multiply $P_\theta(x, z^*, 0)$ by $e^{j\pi\hat{k}_z\, x\, tan\theta}$. Apply the inverse Fourier transform along the $\hat{k}_z$-axis to obtain the final $P_\theta(x, \hat{z}, 0)$.

2.2 Related Work

As discussed previously, CPWC imaging involves collecting a large amount of raw channel (sensor array) data denoted by $RF(x, t, \theta)$, where $x, t,$ and θ correspond to the sensor position, sampling time instance, and PW emission angle, respectively. The key challenge is that how one can reduce the amount of acquired 3-D raw data $RF(x, t, \theta)$, while still getting good-quality final (i.e., beamformed and compounded) 2D image data denoted by $BF(z, x)$. The most notable approaches in this regard are compressed sensing (CS), finite rate of innovation (FRI), angle data driven techniques, etc.

In [45], Tur *et al*. introduced a new sampling approach called the finite rate of innovation (FRI). In this model, they take advantage of the stream of short pulses within a signal (from one sensor) and sample them at a rate much lower than the Nyquist rate, based on the fact that such pulses only need a small number of parameters to fully describe the signals in question: time delay and amplitude. Through the design of a compact class of filters, they managed to represent each pulse by two samples to achieve a stable recovery even with the

presence of a large number of pulses, and they showed that the sampling rate can be reduced 8-fold compared to the Nyquist rate. In [32], Wagner *et al*. extended [45] and proposed an approach called compressed beamforming, where they combined the finite rate of innovation model with CS [57] and Xampling [56] to apply it to multiple sensors of the transducer array. They managed to reduce the number of samples by 8-fold, in the data acquisition phase, needed to reconstruct high energy reflectors, however in exchange, they failed to preserve the speckle information. To correct that, Chernyakova *et al*. in [33] proposed a general concept of compressed beamforming in the frequency domain, where they experimented with sub-Nyquist sampling using CS. They managed to achieve a sampling rate reduction of 28-fold compared to standard beamforming techniques. Furthermore, in [34], Quinsac *et al*. suggested multiple strategies to apply CS to sample signals below the traditional Nyquist sampling rate. They thoroughly studied the different parameters of CS and their applications in the frequency domain to determine the feasibility of CS in ultrasound imaging. For instance, they proposed to use a basis of Diracs as the sampling mask and a Fourier transform as the sparse basis. They managed to achieve up to 75% sample savings, but they also emphasized the need for technological improvements (GPU processing capabilities) to preserve the real-time nature of ultrasound imaging.

In [35], Chen *et al*. introduced the concept of compressive deconvolution in ultrasound imaging to overcome the limitations of the bandwidth of the transducer and the challenges of the physical properties of ultrasound wave propagation. They proposed to reconstruct RF images from compressed measurements by solving a regularized inverse problem that combines random projections and 2D convolution with a spatially invariant point spread function and using the Alternating Direction Method of Multipliers (ADMM) as their

optimization method. They managed to improve the accuracy and the computational time compared to standard compressive sensing methods. In [21], Besson *et al*. applied a regularized compressed beamforming method in the frequency domain by adapting a Fourier-based beamforming inverse problem and implementing appropriate sparse models. They also implemented a 2D Non-Uniform Fourier Transform (NUFT) to compute the Fourier transform in a new migrated (k_x, k_z) discrete space using the UFSB technique. Their results showed considerable artifact reductions (noises and side lobes) which increased the quality of their final displayed image (namely the contrast) compared to classical CS methods. In [36], the authors compared their sparse regularization from [21] to Lu's and Garcia's methods, and verified the superiority of their UFSB-based approach in terms of image quality.

In [51], Besson *et al*. presented two different techniques for data acquisition taking advantage of fast and matrix-free formulations derived for the measurement model and its adjoint, as well as the sparse nature of ultrasound images in certain representation bases. Using a sparse regularization framework, they managed to reduce the computation cost by three orders of magnitude (in comparison with state-of-the-art ultrasound compressive sensing methods) as well as improve the overall image quality. In [50], Schretter *et al*. propose a different compressive sensing scheme to tackle ultrasound data acquisition and image reconstruction. At the acquisition phase, their technique involves the use of point spread functions (PSF) that represent echo responses from isolated points in the insonified medium, to form a dictionary of shift-variant bent waves. Their strategy, called importance-weighted random sampling, resulted in fewer RF data samples (by enforcing a sparsity model). At the reconstruction stage, they use Moore-Penrose pseudo-inverse method to

enhance the image reconstruction process using a precomputed minimum-norm inversion solver. Simulation results demonstrated that they managed to obtain high quality images with fewer data points, in order to provide a practical solution for recovering volumetric ultrasound images from large phased-array probes. In [52], Ozkan *et al.* devised an inverse problem (IP) approach for ultrasound beamforming, by defining a linear forward model and solve its ill-posed IP with a regularized based technique (least squares method) that implements different regularization constraints. The forward model is based on the geometry of the transducer and sound travel assumptions. The proposed techniques achieved excellent full-width at half-maximum and contrast to-noise ratio values, using only a single plane-wave emission. In [8], Akbar *et al*. proposed an angle selection method guided by beamformed data similarity measurements. They created a recursive angle selection function that dynamically compares already beamformed data to new ones to decide whether or not an additional PW emission at a different angle is needed. Using the reference 75-PW data set, they have demonstrated that comparable resolution and contrast can be achieved using only 13-18 PWs.

Recently, research interest has shifted towards deep learning ultrasound imaging. For instance, Khan *et al*. [37] show that a universal deep beamformer could be trained to generate high quality images over wide varying aperture and channel subsampling patterns. This universal beamformer utilizes a deep learning framework designed to process sub-sampled RF data acquired at different subsampling rates and then detect the general data configuration to generate the final images. In [39], the same authors focused on applying a deep neural network to directly process full or subsampled RF signals at various sub sampling rates. In [38], Van Sloun *et al*. provide a comprehensive survey of different deep

learning strategies in the context of ultrasound imaging that address both the structure of ultrasound signals (possible sparsity in a chosen basis) and data dimensionality reduction.

In this thesis, we propose a simple method that significantly reduces the acquisition cost of the raw RF data. Our scheme provides an alternative to computationally expensive techniques (such as CS), relying on deterministic subsampling that follows power level patterns in the zero-angle raw data frame. We should mention that while our imaging results demonstrate improvements in terms of resolution, they suffer from contrast degradation caused by the subsampling effects.

Chapter 3: Proposed Subsampling Approach

In this chapter, we will explain the details of our proposed approach.

Recall that ultrafast plane-wave ultrasound imaging [11] typically involves acquiring a 3D raw dataset $RF(t,x,\theta)$ by a transducer array, where θ denotes the steering angle of an emitted PW pulse (giving rise to the backscattered signals to be sampled), x refers to the individual sensor positions within the array, and t represents the sampling time instance. After beamforming and coherent compounding, we get a 2D compounded image dataset $D(z,x)$, where $z = ct/2$ is the imaging depth, and c is the speed of sound in the insonified medium.

Our main objective is to reduce the amount of sensor array data recorded in $RF(t,x,\theta)$, while producing acceptable-quality $D(z,x)$ images. Instead of using a CS technique, we first acquire zero-angle $RF(t,x,\theta = 0)$ in full, from which we derive deterministic subsampling patterns for the remaining nonzero-angle raw data. Next, we subsample $RF(t,x,\theta \neq 0)$ accordingly, then beamform the acquired samples, and finally, compound the resulting beamformed data to produce $D(z,x)$. To reconstruct the image, we are using a Fourier-based technique described in chapter 2. In the sequel, we have changed $\hat{k}_z$ to k_z for convenience.

For each angle θ, we first transform the corresponding 2D raw data denoted by $P_\theta(t,x)$ into its spectrum $F_\theta(f,k_x)$ (note that $P_\theta(t,x)$ is simply a 2D "slice" of $RF(t,x,\theta)$ for a particular value of θ). Next, we remap the f-axis data into the k_z-axis data via linear interpolation, which yields the migrated spectrum $K_\theta(k_z,k_x)$. Then, we transform the latter into its (k_z,x)-domain representation (via the inverse Fourier transform along the k_x-axis),

and multiply the result element-wise by exp $(j\pi k_z x\ tan(\theta))$, thus producing the phase-shifted spectrum $S_\theta(k_z, x)$. Finally, we compound all of such θ-specific spectra $S_\theta(k_z, x)$ by adding them together (i.e., summing over a given set of θ values), and then apply the inverse Fourier transform along the k_z-axis to obtain $D(z, x)$.

The spectral remapping (mentioned in chapter 2) is performed using the following formulas [30]:

$$K_\theta(k_z, k_x) = A(k_z, k_x, \theta).F_\theta\big(f_{mig}(k_z, k_x, \theta), k_x\big), \tag{3.1}$$

$$f_{mig}(k_z, k_x, \theta) = \frac{ck_z}{1 + cos\theta}\left[1 + \left(\frac{k_x}{k_z}\right)^2\right], \tag{3.2}$$

$$A(k_z, k_x, \theta) = \frac{c}{1 + cos\theta}\left[1 - \left(\frac{k_x}{k_z}\right)^2\right]. \tag{3.3}$$

3.1 Acquisition Scenario

Let N_t, N_x, and $N_a$denote the number of sampling time instances, the number of sensors (channels), and the number of PW emission angles, respectively. The full acquisition of $RF(t, x, \theta)$ would entail collecting as many as $N_t \times N_x \times N_a$ samples. We want to reduce the total number of acquired raw data samples, while still aiming to produce acceptable-quality[1] compounded images. We begin the acquisition process by fully sampling the zero-angle 2D raw RF data denoted by $P_0(t, x)$, i.e., our initial cost is $N_t \times N_x$ samples. Then, for each $\theta \neq 0$, we are to acquire some fraction $p < 1$ of the corresponding 2D raw RF

[1] Our notion of "acceptable quality" refers to certain image quality metrics (such as the CNR and FWHM values) being within some expected ranges that arise from the full-acquisition cases (serving as a baseline). Further details are provided in section 4.1.2.

data denoted by $P_\theta(t,x)$. The total cost will then become: $N_t \times N_x + p \times (N_a - 1)$ samples, which implies the savings of $\frac{1+p\times(N_a-1)}{N_a} \times 100\%$.

We let $P_\theta{}^*(t,x)$ denote a subsampled representation of $P_\theta(t,x)$, and $M_\theta(t,x)$ a binary sampling matrix for $P_\theta(t,x)$. If we have $M_\theta(t_m,x_l) = 1$ for some specific location (t_m,x_l) within our sampling grid $(m = 1,2,\dots,N_t,\ l = 1,2,\dots,N_x)$, then $P_\theta{}^*(t_m,x_l) = P_\theta(t_m,x_l)$; otherwise, $P_\theta{}^*(t_m,x_l) = 0$. We can express such subsampling compactly as:

$$P_\theta{}^*(t,x) = M_\theta(t,x) \odot P_\theta(t,x), \qquad (3.4)$$

where $\odot$ denotes the element-wise multiplication. The total number of ones in $M_\theta(t,x)$ is equal to $N_p = p \times (N_t \times N_x)$.

Given multiple θ-specific $P_\theta{}^*(t,x)$ as inputs, we apply our Fourier-domain reconstruction sequence from [30] to all of them individually, which is then followed by compounding (over all nonzero θ values) and computing the analytic signal (out target output) via the Hilbert transform:

$$P_\theta{}^*(t,x) \to F_\theta{}^*(f,k_x) \to K_\theta{}^*(k_z,k_x) \to S_\theta{}^*(k_z,x),$$

$$\sum_{\theta\neq 0} S_\theta{}^*(k_z,x) \to H^*(z,x)$$

The zero-angle data $P_0(t,x)$, acquired in full, yields:

$$P_0(t,x) \to F_0(f,k_x) \to K_0(k_z,k_x) \to S_0(k_z,x) \to H_0(z,x)$$

Finally, our target output $H(z,x)$ is estimated as follows:

$$\widehat{H}(z,x) = H^*(z,x) + H_0(z,x) + \widetilde{H}(z,x) \qquad (3.5)$$

where $\widetilde{H}(z,x)$ serves as an auxiliary "data filler" to mitigate the negative impact of subsampling. In the worst case, $\widetilde{H}(z,x)$ is simply all zeros. In the best case, it provides an adequate approximation of unknown $\overline{H}^*(z,x)$ that represents what we would have obtained from the missing data:

$$\bar{P}_\theta{}^*(t,x) \to \bar{F}_\theta{}^*(f,k_x) \to \bar{K}_\theta{}^*(k_z,k_x) \to \bar{S}_\theta{}^*(k_z,x),$$

$$\sum_{\theta\neq 0} \bar{S}_\theta{}^*(k_z,x) \to \overline{H}^*(z,x).$$

Here each "hypothetical" $\bar{P}_\theta{}^*(t,x)$ contains the data samples from $P_\theta(t,x)$ that are not in $P_\theta{}^*(t,x)$. Equivalently:

$$\bar{P}_\theta{}^*(t,x) = \bar{M}_\theta(t,x) \odot P_\theta(t,x), \qquad (3.6)$$

where $\bar{M}_\theta(t,x)$ is the complemented version of binary $M_\theta(t,x)$. Since:

$$\bar{P}_\theta{}^*(t,x) = P_\theta(t,x) - P_\theta{}^*(t,x), \qquad (3.7)$$

we get:

$$H(z,x) - \widehat{H}(z,x) = \overline{H}^*(z,x) - \widetilde{H}(z,x), \qquad (3.8)$$

which stresses the importance of $\widetilde{H}(z,x)$ being close to the unknown $\overline{H}^*(z,x)$.

3.2. Sampling Mask Derivation

The main idea of this work pertains to the derivation of the θ-specific sampling pattern matrices $M_\theta(t,x)$ from the zero-angle information stored in $P_0(t,x)$. The first step is to identify which N_p data samples in $P_0(t,x)$ are deemed most useful: for example, we may select those having the largest absolute values. Next, we record their corresponding

locations as ones in our initial zero-angle matrix $M_0(t,x)$, and then generate its (k_z,x)-domain representation denoted by $S_0^M(k_z,x)$:

$$M_0(t,x) \rightarrow F_0^M(f,k_x) \rightarrow K_0^M(k_z,k_x) \rightarrow S_0^M(k_z,x) \qquad (3.9)$$

For any given $\theta \neq 0$, the binary sampling matrix $M_\theta(t,x)$ can now be obtained from $S_0^M(k_z,x)$ as follows: We multiply $S_0^M(k_z,x)$ element-wise by $exp(-j\pi k_z x tan(\theta))$, transform it into its (k_z,k_x)-domain version, and perform demigration (i.e., we remap from f_{mig} back to f, thus producing a particular θ-specific (f,k_x) spectrum. Then, we apply the inverse Fourier transform to the said spectrum, which yields the desired (t,x)- domain matrix $\widetilde{M}_\theta(t,x) \approx M_\theta(t,x)$. To get our final $M_\theta(t,x)$, we simply binarize $\widetilde{M}_\theta(t,x)$ via thresholding: for example, the first N_p largest-magnitude elements of $\widetilde{M}_\theta(t,x)$ become 1,while the rest are set to 0. Essentially, $S_0^M(k_z,x)$ goes through the reconstruction sequence shown in equation (3.9) in reverse, except that $\theta \neq 0$ is now incorporated into the corresponding remapping equations.

3.3. Data Filler Possibilities

As mentioned above, $\widetilde{H}(z,x)$ serves as an auxiliary "data filler" to mitigate the negative impact of subsampling and to approximate the unknown $\bar{H}^*(z,x)$. We have explored six possibilities to enhance and improve this data filler, as described below.

3.3.1. Option A: No Extra Data

In this case, we let:

$$\widetilde{H}(z,x) = \frac{\|H^*(z,x) + H_0(z,x)\|_2}{\|H_0(z,x)\|_2} \bar{H}_0^*(z,x), \qquad (3.10)$$

where $\bar{H}_0^*(z,x)$ denotes the reconstruction result for the input $\bar{P}_\theta^*(t,x) = \bar{M}_0(t,x) \odot P_0(t,x)$ that simulates the "missing" portion of the initial zero-angle raw RF data frame (i.e., as if it underwent $M_0(t,x)$-based subsampling). The multiplication factor in (3.10) accounts for the energy content difference arising due to compounding.

3.3.2. Option B: Extra Data via 2D Uniform Subsampling

Our goal here is to acquire additional data samples from $\bar{P}_\theta^*(t,x)$ via uniform 2D down-sampling (i.e., along both t-axis and x-axis), get the respective analytic-signal output (via the Hilbert transform), and add it to our data filler formula to enhance $\tilde{H}(z,x)$. In this case, we focus on $\bar{P}_\theta^*(t,x)$ that contains data samples from $P_\theta(t,x)$ not present in $P_\theta^*(t,x)$. We begin by "simulating" regular down-sampling of $\bar{P}_\theta^*(t,x)$ (also known as decimation) by the integer factors S_t and S_x on $\bar{P}_\theta^*(t,x)$ along t-axis and x-axis as follows:

$$\bar{P}_{\theta_d}^*(t_d, x_d) = \bar{P}_\theta^*(S_t t, S_x x), \qquad (3.11)$$

where $\bar{P}_{\theta_d}^*(t_d, x_d)$ is our acquired (regularly subsampled) data. Note that such decimation will decrease the dimensionality of $\bar{P}_{\theta_d}^*(t_d, x_d)$ by S_t x S_x, compared to $\bar{P}_\theta^*(t,x)$, as shown in Figure 3.1.

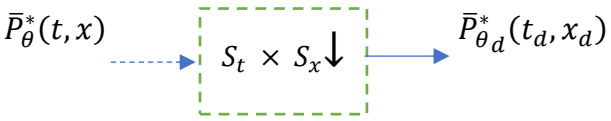

Figure 3.1: Down-sampling operation.

To rectify this, we up-sample the signal $\bar{P}_{\theta_d}^*(t_d, x_d)$ to obtain $\bar{P}_{\theta_u}^*(t,x)$ by the same subsampling factors S_t and S_x, i.e.,

$$\bar{P}^*_{\theta_u}(t,x) = \bar{P}^*_{\theta_d}\left(\frac{t_d}{S_t}, \frac{x_d}{S_x}\right). \qquad (3.12)$$

Essentially, we insert zeros for the missing samples so that dim $\bar{P}^*_{\theta_u}$ = dim $\bar{P}^*_{\theta}$ as shown in Figure 3.2.

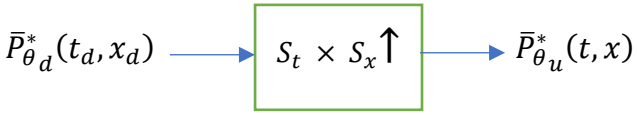

Figure 3.2: Up-sampling operation.

Figure 3.3 summarizes the steps performed to obtain an additional spectral component $\bar{F}^*_{\theta_u}(f, k_x)$ from extra data samples acquired via uniform subsampling.

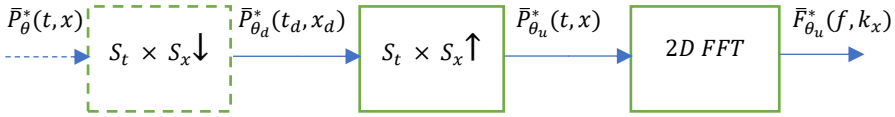

Figure 3.3: Uniform subsampling.

Once we obtain $\bar{F}^*_{\theta_u}(f, k_x)$, we follow the usual processing flow to get the associated target output $\bar{H}^*_{\theta_u}(z,x)$ for all $\theta \neq 0$:

$$\bar{F}^*_{\theta_u}(f, k_x) \rightarrow \bar{K}^*_{\theta_u}(k_z, k_x) \rightarrow \bar{S}^*_{\theta_u}(k_z, x),$$

$$\sum_{\theta \neq 0} \bar{S}^*_{\theta_u}(k_z, x) \rightarrow \bar{H}^*_{\theta_u}(z,x).$$

Then, our estimate of the target output $\hat{H}(z,x)$ becomes:

$$\hat{H}(z,x) = H^*(z,x) + H_0(z,x) + \bar{H}^*_{\theta_u}(z,x) + \tilde{H}(z,x), \qquad (3.13)$$

where our data filler $\widetilde{H}(z,x)$ is now given by:

$$\widetilde{H}(z,x) = \frac{\left\|H^*(z,x) + \bar{H}^*_{\theta_u}(z,x) + H_0(z,x)\right\|_2}{\|H_0(z,x)\|_2}\bar{H}^*_0(z,x) \qquad (3.14)$$

3.3.3. Option C: Extra data via 2D Random Subsampling

As opposed to 2D uniform subsampling, 2D random subsampling selects data samples at random. In our case, we are to select extra data samples from $\bar{P}^*_\theta(t,x)$ randomly, rather than at regular intervals.

Let $\bar{P}^*_{\theta_r}(t,x)$ represent our randomly subsampled data. Then, the associated target output can be computed as follows:

$$\bar{P}^*_{\theta_r}(t,x) \rightarrow \bar{F}^*_{\theta_r}(f,k_x) \rightarrow \bar{K}^*_{\theta_r}(k_z,k_x) \rightarrow \bar{S}^*_{\theta_r}(k_z,x)$$

$$\sum_{\theta \neq 0} \bar{S}^*_{\theta_r}(k_z,x) \rightarrow \bar{H}^*_{\theta_r}(z,x)$$

Our estimate of the target output $\widehat{H}(z,x)$ becomes:

$$\widehat{H}(z,x) = H^*(z,x) + H_0(z,x) + \bar{H}^*_{\theta_r}(z,x) + \widetilde{H}(z,x), \qquad (3.15)$$

where, our data filler $\widetilde{H}(z,x)$ in now given by

$$\widetilde{H}(z,x) = \frac{\left\|H^*(z,x) + \bar{H}^*_{\theta_r}(z,x) + H_0(z,x)\right\|_2}{\|H_0(z,x)\|_2}\bar{H}^*_0(z,x) \qquad (3.16)$$

3.3.4. Option D: Extra data via 1-D Random Subsampling with Sparse Recovery

This option aims to recover the full Fourier spectrum $\bar{F}_\theta^*(f, k_x)$ utilizing 1-D random subsampling of $\bar{P}_\theta^*(t, x)$ along the t-axis. Such recovery follows the compressive sensing (CS) paradigm and involves sparsity-promoting optimization [46].

As Liebgot *et al*. stated in [40], compressive sensing allows the reconstruction of a length-n signal $x \in R^n$, from a length-m signal $y \in R^m$, such that y is a linear random combination of x and that $m < n$. Typically, y is acquired through a sensing basis ϕ such that:

$$y = \phi x, \qquad (3.17)$$

where ϕ is an m x n matrix. For instance, in MRI, ϕ is the Fourier basis, and in ultrasound imaging, ϕ is often an excerpt of the identity matrix [58].

Additionally, the original signal x should be expanded in an orthonormal (or representation) basis Ψ (Fourier, wavelets, wave atoms, etc.), such that:

$$x = \Psi v, \qquad (3.18)$$

where v is the coefficient vector of this representation. It is assumed that v is s-sparse, i.e., the number of non-zero elements s of v is small: $s < m < n$.

It is possible to recover v with a very high probability, provided that ϕ and Ψ are mutually incoherent [43]. The problem could be written now as:

$$y = \phi\Psi v = \mathrm{A}v, \qquad (3.19)$$

where A is an $m\ x\ n$ full-rank matrix (all rows of A are independent).

Once v is estimated based on equation (3.19), signal x can be computed using equation (3.18). Candes *et al*. [41] showed that solving equation (3.19) is feasible through an optimization problem $P0$ stated below.

$$P0: \qquad \hat{v} = argmin_{v \in R^n} \|v\|_0 \quad subject\ to \quad y = Av, \qquad (3.20)$$

where the l_0 pseudo-norm is defined as $\|v\|_0 = |\{i, v_i \neq 0\}|$.

Another approach by Candes *et al*. [42] imposes certain restrictions on the full rank matrix A (on its isometry constant to be exact), which allows to estimate v by solving problem $P1$ stated below.

$$P1: \qquad \hat{v} = argmin_{v \in R^n} \|v\|_1 \quad subject\ to \quad y = Av, \qquad (3.21)$$

where the l_1 norm is defined as $\|v\|_1 = \sum_{i=1}^{n} |v_i|$.

In our case, we adopt P1 to compute the CS estimate of $\bar{F}_\theta{}^*(f, k_x)$, obtained from additional randomly sampled data entries captured in $\bar{P}^*_{\theta_r}(t, x)$. Specifically, we perform the following steps:

Step 1: Apply 1D Fourier transform to $\bar{P}^*_\theta(t, x)$ along the x-axis to obtain the (t, k_x) spectrum.

Step 2: Generate the representation basis Ψ, which is the Fourier transform matrix of size N_t.

Step 3: Generate the sensing basis ϕ, which is the random permutation of s rows $(s < < N_t)$ of the identity matrix of size N_t.

Step 4: Multiply ϕ and Ψ to form matrix A from equation (3.19).

Step 5: For the signal in the (t, k_x) spectrum obtained in step 1, multiply Ψ with each of this signal's columns, which corresponds to vector v from equation (3.18).

Step 6: Multiply matrix A with the resulting signal from step 5 to obtain y from equation (3.19).

Step 7: Obtain the initial solution x_0, by multiplying the transpose of matrix A with vector y.

Step 8: Apply the "l1eq_pd" primal-dual algorithm from the L1-MAGIC package [46] to solve the P1-type problem stated above and obtain $\bar{F}_{\theta}{}^{*}_{cs_i}(f, k_x)$ for each column i, where $i = 1, \dots, N_x$. This algorithm is subject to predefined number of primal-dual iterations $pdmaxiter$ and a duality gap $pdtol$ as a tolerance factor for the primal-dual algorithm.

Step 9: Repeat steps 5-9 N_x times to obtain a complete $\bar{F}_{\theta}{}^{*}_{cs}(f, k_x)$ spectrum.

Once we recover $\bar{F}_{\theta}{}^{*}_{cs}(f, k_x)$ for all nonzero-θ data frames, we compute compounded $\bar{H}_{\theta}{}^{*}_{cs}(z, x)$ as usual. Then, our estimate of the target output $\widehat{H}(z, x)$ becomes:

$$\widehat{H}(z,x) = H^*(z,x) + H_0(z,x) + \bar{H}_{\theta_{cs}}{}^{*}(z,x) + \widetilde{H}(z,x), \qquad (3.22)$$

where, our data filler $\widetilde{H}(z, x)$ is now given by

$$\widetilde{H}(z,x) = \frac{\left\| H^*(z,x) + \bar{H}_{\theta_{cs}}{}^{*}(z,x) + H_0(z,x) \right\|_2}{\|H_0(z,x)\|_2} \bar{H}_0^*(z,x) \qquad (3.23)$$

3.3.5. Option E: No Extra Data with Target Output Masking

This option attempts to enhance our data filler by deriving a target output binary mask, denoted by $H_{mask}\ (z,x),$ based on the zero-angle frame $H_0(z,x)$. Specifically, we perform the following steps:

Step 1: We take the absolute value of $H_0(z,x)$ to obtain the envelope denoted by $absH_0(z,x)$.

Step 2: To preserve the content of $absH_0(z,x)$, we smooth it by applying an appropriate filter to obtain $absH_0(z,x)_{smooth}$. In our case, we apply a median filter. As stated in [48] and [61], this is a standard post-filtering technique that uses the median intensity in a determined sized and shaped region W_{ij} that surrounds the pixel (i,j) of interest to eliminate any impulsive artifacts with an area (in pixels) less than half the region size $\|W_{ij}\|$.

Step 3: We binarize $absH_0(z,x)_{smooth}$ to get target output $0-1$ mask $H_{mask}\ (z,x)$. This is accomplished by adaptive thresholding that chooses localized thresholds to minimize the intraclass variance of the thresholded black and white pixels [59]. For each pixel, a threshold is computed by applying a local mean intensity around the neighborhood of the pixel. The threshold luminance value is a scalar between 0 and 1.

Consequently, our data filler $\widetilde{H}(z,x)$ becomes:

$$\widetilde{H}(z,x) = \frac{\|H^*(z,x)+H_0(z,x)\|_2}{\|H_0(z,x)\|_2}\,\overline{H}_0^*(z,x)\ H_{mask}\ (z,x). \qquad (3.24)$$

3.3.6. Option F: No Extra Data with Fourier-Based Target Output Masking

Similar to option E, this option aims to generate $H_{mask}\ (z,x)$ through smoothing the zero-angle envelope $absH_0(z,x)$ in the Fourier domain instead. Specifically, we execute the same steps shown in option E, but instead of using a median filter (to generate $absH_0(z,x)_{smooth}$), we apply a homomorphic filter. This type of filtering targets multiplicative noise (as opposed to additive noise targeted by other types of filters). It first computes the natural logarithm of the input signal, so that the noise component becomes additive, as per the following equation [49]:

$$\ln\left(absH_0(z,x)\right) = \ln\big(absH'_0(z,x)\big) + \ln\big(n(z,x)\big), \qquad (3.25)$$

where $n(z,x)$ is the multiplicative noise in the signal. The homomorphic filtering process is performed in the Fourier domain by taking the frequency response of $absH_0(z,x)$, and then applying a low pass filter. We use a Butterworth filter defined by:

$$H(u,v) = \frac{1}{1+\left[\frac{W}{W_0}\right]^{2n}}, \qquad (3.26)$$

where W_0 is the cutoff frequency, and n is the order of the filter. To obtain the filtered output signal, we take the inverse Fourier transform followed by exponentiation, to compensate for the logarithmic transformation of the input signal. Figure 3.4 summarizes this idea.

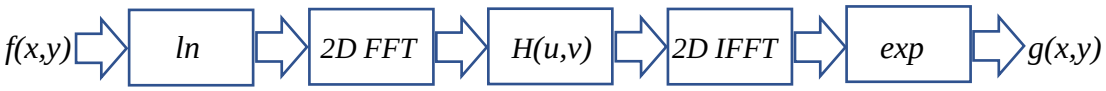

Figure 3.4: Sequence of steps in homomorphic filtering [49].

Note that $f(x,y)$ here corresponds to $absH_0(z,x)$ and $g(x,y)$ corresponds to $absH_0(z,x)_{smooth}$. Consequently, our data filler $\widetilde{H}(z,x)$ becomes similar to (3.24).

Chapter 4: Evaluation Results

4.1 PICMUS Evaluation Setup

Our evaluation setup is based on the Plane-wave Imaging Challenge in Medical UltraSound (PICMUS) evaluation framework [47], which is designed specifically for coherent plane-wave compounding (CPWC) imaging and provides standardized evaluation routines to compare different beamforming methods [18]. PICMUS offers two experimental CPWC datasets generated from real acquisitions using a Versonics Vantage 256 research scanner equipped with an L11-4v linear array probe [47], [18]. Figure 4.1 shows the imaged regions of a CIRS Multi-Purpose Ultrasound Phantom [18]: the highlighted left region corresponds to two anechoic cysts phantoms distributed vertically, while the highlighted right region corresponds to seven isolated scatterers (point phantoms), distributed vertically and horizontally. Both regions include hyperechoic structures with different grayscale intensity (see Figure 4.1) and a fully developed speckle background. For our evaluation results, we will focus on these two regions to test the contrast of the cyst phantoms and the resolution of the point phantoms, as well as the speckle quality, for each of our proposed data filler options. For the rest of our evaluation discussion, TYPE-1 images refer to those with the anechoic cysts, while TYPE-2 images refer to those with the point phantoms.

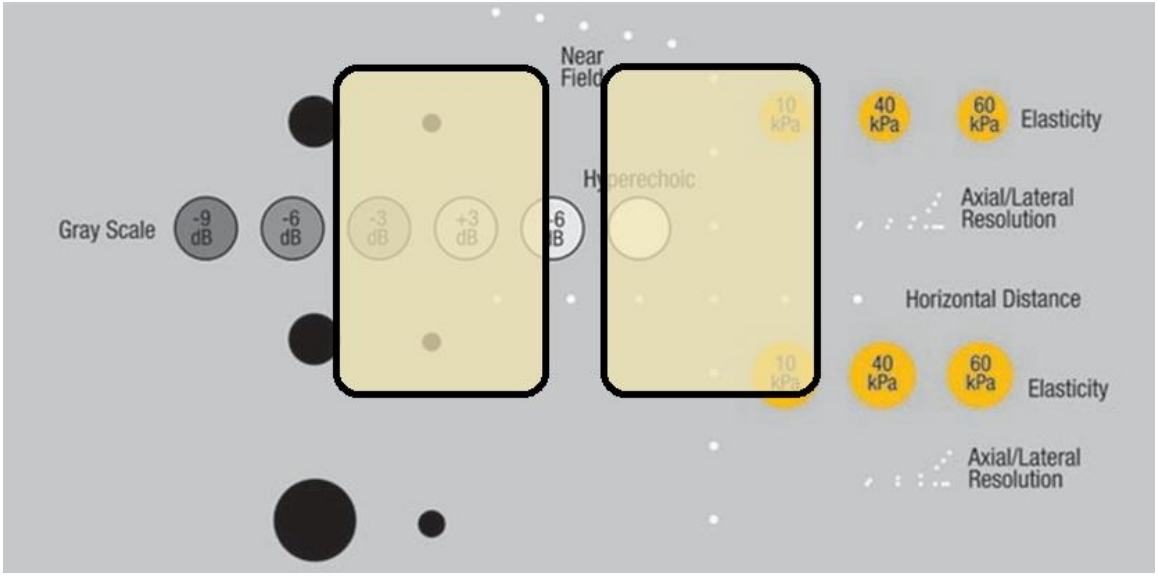

Figure 4.1: Schematic of the upper part of the CIRS Model 040GSE Phantom used to collect the experimental data. The highlighted left region was acquired for contrast evaluation, while the highlighted right region was acquired for resolution evaluation [18].

4.1.1 Description of Datasets and Metrics

Each PICMUS dataset consists of 75 θ-specific plane waves whose emission angle θ ranges between -16° and 16° with an angle increment of 0.43°. Each plane wave represents a 2D RF data frame of size 1536-by-128, where 1536 is the number of sampling time instances at which the sensor measurements are taken per second and 128 is the number of sensors in the array transducer. Table 4.1 shows real experimental parameters related to the probe settings.

Table 4.1: PICMUS experimental data acquisition parameters [18]

Pitch	0.30 mm
Transducer element width	0.27 mm
Transducer element height	5 mm
Number of elements (channels)	128
Aperture width	38.4 mm
Elevation focus	20 mm
Transmit frequency	5.208 MHz
Sampling frequency	20.832 MHz
Pulse bandwidth	67%
Excitation	2.5 cycles

Our evaluation metrics are based on [47] and are as follows:

- The contrast-to-noise ratio (CNR), which is measured for the top/bottom anechoic cyst regions (two anechoic cylinder targets) in data TYPE-1 images, as shown in Figure 4.2 (a) and (b). The CNR values are given by the equation below:

$$CNR = 20log_{10}\left(\frac{|\mu_{in} - \mu_{out}|}{\sqrt{\frac{(\sigma_{in}^2 - \sigma_{out}^2)}{2}}}\right), \quad (4.1)$$

  where μ_{in} is the average signal level inside the anechoic cyst region, μ_{out} is the average signal level in the surrounding background, σ_{in} and σ_{out} are the standard deviations inside and outside the anechoic cyst region. We should note that higher CNR values are associated with higher image quality.

- Speckle quality, which is often used for tissue classification, structure segmentation, motion estimation, etc. [47]. Speckle quality is assessed via the Kolmogorov-Smirnov (KS) tests for speckle preservation, to verify whether the data follows a Rayleigh distribution by testing the specified regions in Figure 4.2 (d) and Figure 4.3 (c) against a certain significance level α. Speckle regions with α equal to 0.05 are considered as regions with speckle quality preserved.
- The full width at half maximum (FWHM), which is measured for point phantoms (wire targets) as shown in Figure 4.2 (c) and Figure 4.3 (b). For each of these point phantoms, axial and lateral signals passing through the local maximum of intensity are extracted. From those two signals, the full width at half maximum is computed, leading to two measures per point scatterer [47]. We should note that lower FWHM values are associated with higher image quality.

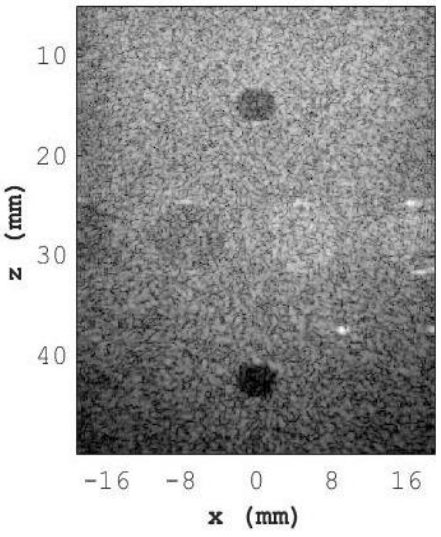

(a)

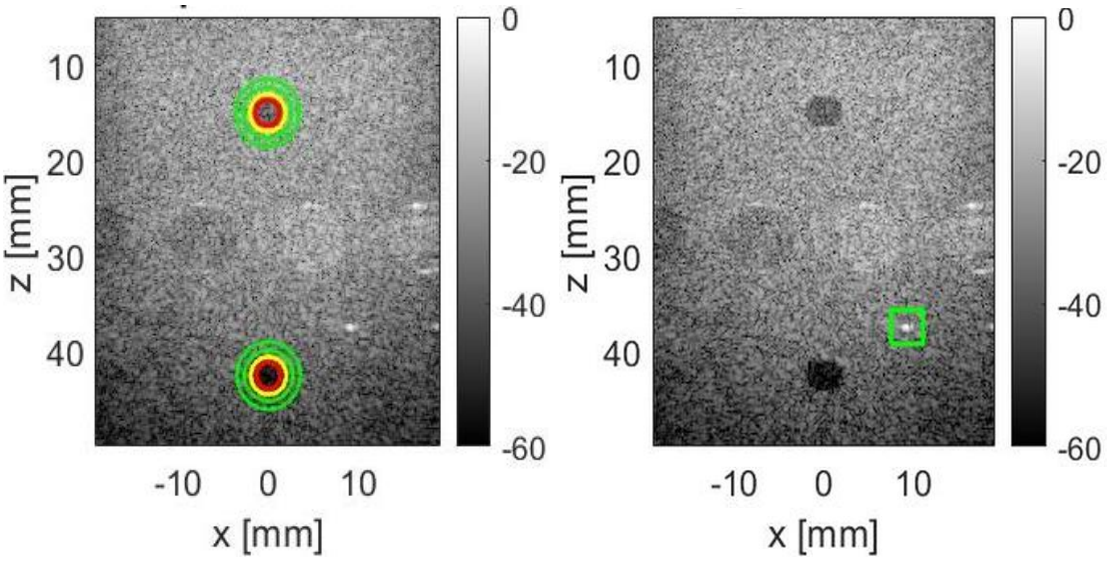

(b) (c)

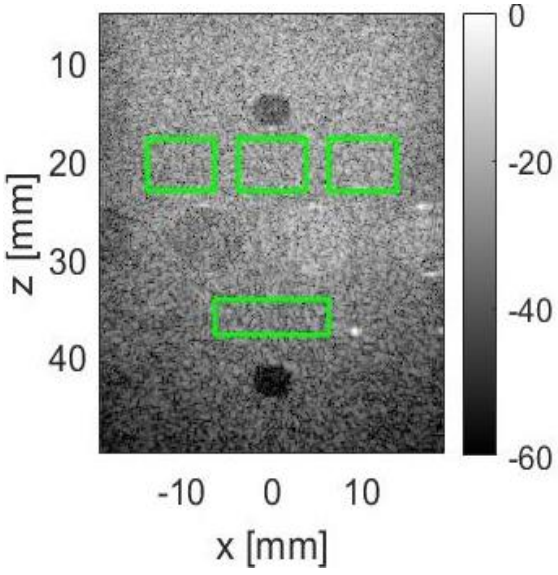

(d)

Figure 4.2: (a) TYPE-1 image with (b) highlighted CNR regions of interest, (c) highlighted FWHM region of interest, and (d) speckle quality test areas

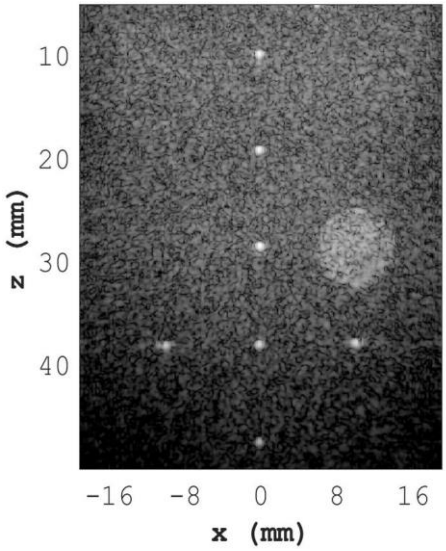

(a)

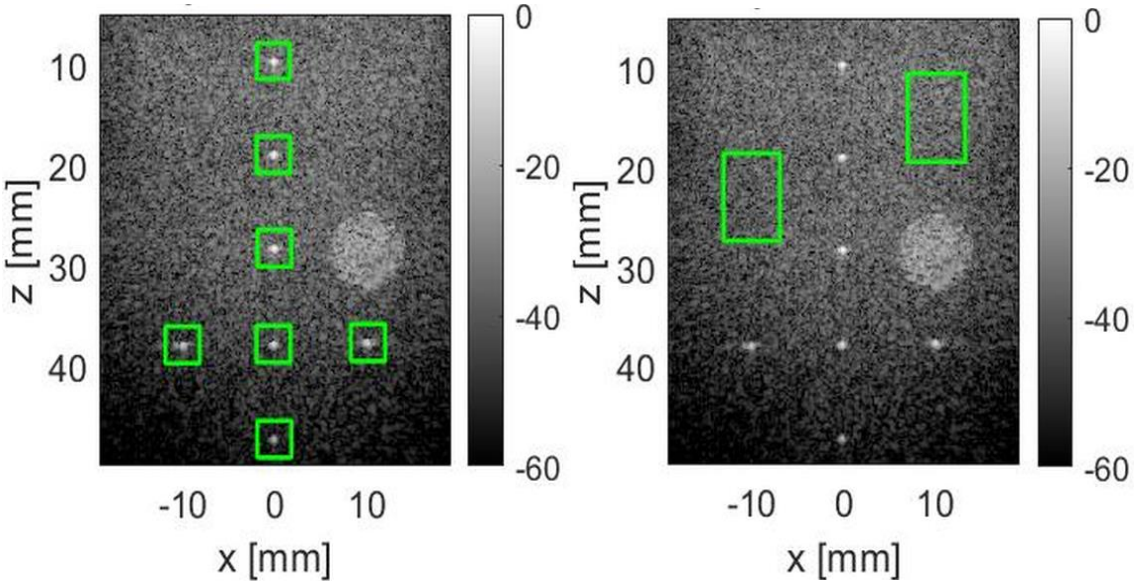

(b) (c)

Figure 4.3: (a) TYPE-2 image with (b) highlighted FWHM regions of interest and, (c) speckle quality test areas

4.1.2 Full Acquisition (FA) Reference Case

To evaluate our proposed subsampling method, we have used $N_a = 5$ PW emissions at 5 equidistant angles from -16° to 16°, and $N_a = 25$ PW emissions at 25 equidistant angles from -16° to 16°. For each θ, the N_t-by- N_x size of raw RF data frames was 1536×128. After reconstruction, we generated the B-mode images by log-compressing their respective normalized envelope sections covering the z-axis range $[5, 50]$ mm, as shown in Figure 4.4 and Figure 4.5. Figure 4.6 shows full-acquisition image for the case of a single PW (zero-angle emission) for comparison purposes.

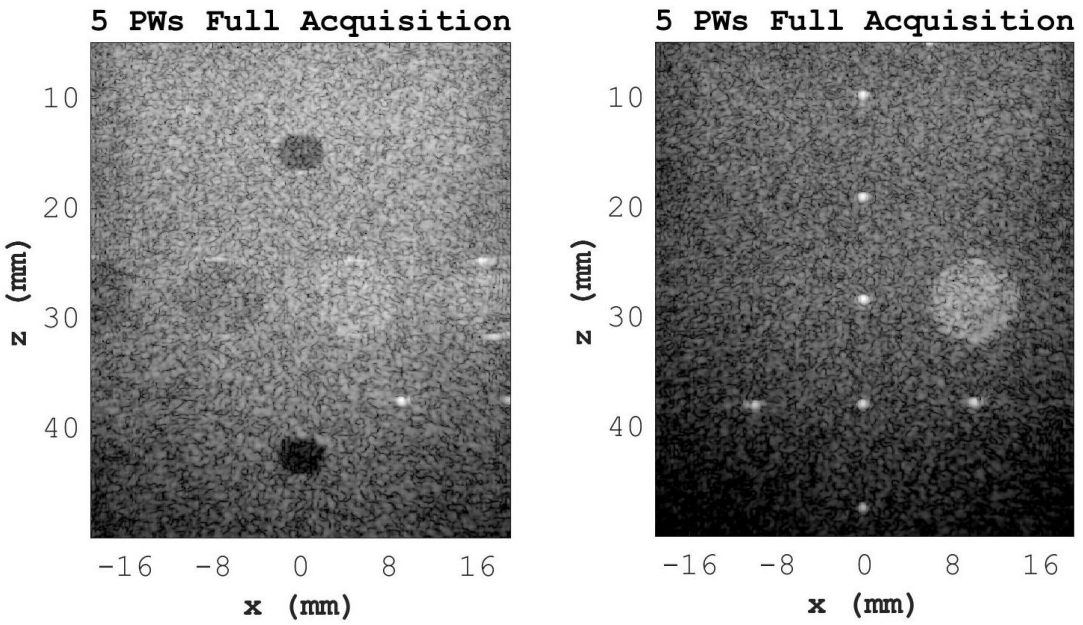

Figure 4.4: Reference TYPE-1 (left) and TYPE-2 (right) compounded images – 5PWs

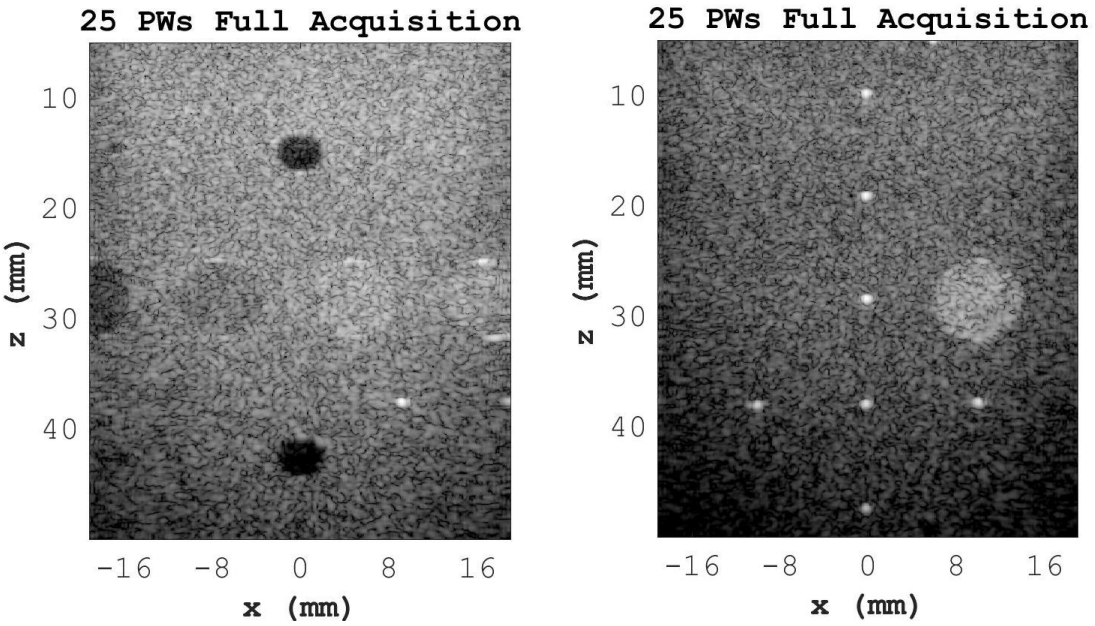

Figure 4.5: Reference TYPE-1 (left) and TYPE-2 (right) compounded images – 25PWs

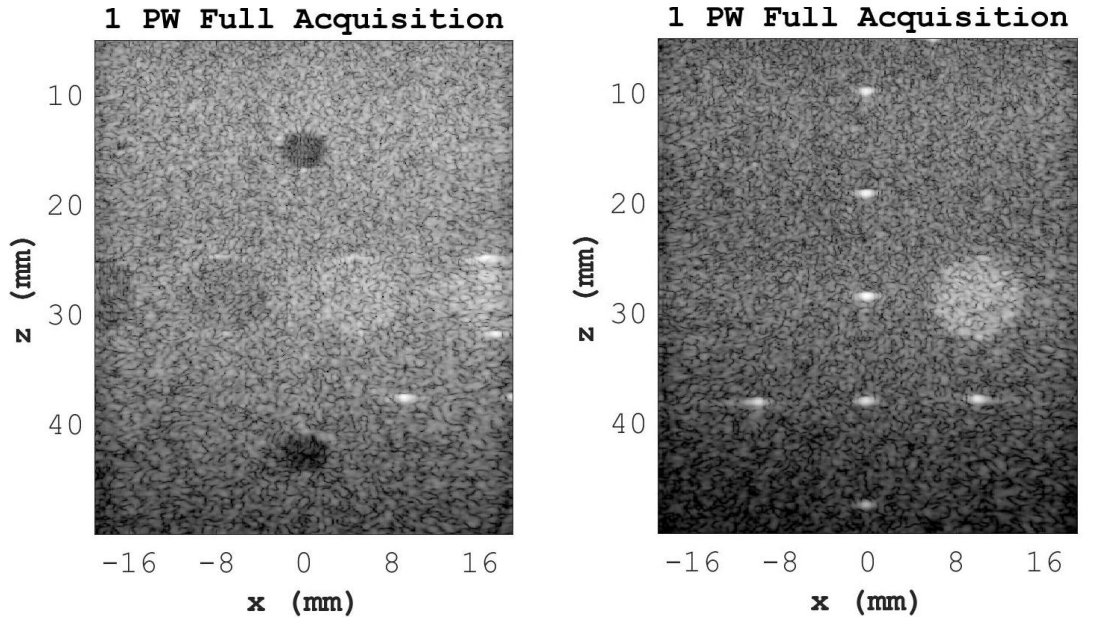

Figure 4.6: Reference TYPE-1 (left) and TYPE-2 (right) initial images – 1PW

Table 4.2 provides a quantitative quality indicator for the TYPE-1 and TYPE-2 images at FA for the 1PW, 5PW, and 25PW cases. Note that the TYPE-2 images are assessed based on the average axial/lateral $\overline{\text{FWHM}}$ computed over all seven-point phantoms.

Table 4.2: FA image quality indicators

Case	TYPE-1			TYPE-2	
	Top/Bottom CNR (dB)	Axial/Lateral FWHM (mm)	Speckle Test	Axial/Lateral $\overline{\text{FWHM}}$ (mm)	Speckle Test
1PW	8.6/6.0	0.48/0.85	Pass 4/4	0.48/0.80	Pass 2/2
5PW	8.0/9.5	0.49/0.48	Pass 4/4	0.47/0.44	Pass 2/2
25PW	12.6/11.7	0.48/0.52	Pass 4/4	0.49/0.51	Pass 2/2

Comparing the 1PW and 5PW entries in Table 4.2, it is reasonable to anticipate that in the 5PW subsampling case, compounding zero-angle full-input reconstruction data with 4 nonzero-angle partial-input reconstruction data would produce the top and bottom CNR values within [8.0, 8.6] dB and [6.0, 9.5] dB, respectively; we would also expect the lateral FWHM values to decrease from 0.80-0.85 mm towards 0.44-0.48 mm. Similarly, comparing the 1PW and 25PW entries, we expect that in the 25PW subsampling case, compounding zero-angle full-input reconstruction data with 24 nonzero-angle partial-input reconstruction data would produce the top and bottom CNR values within [8.6, 12.6] dB and [6.0, 11.7] dB, respectively; we would also expect the lateral FWHM values to decrease from 0.80-0.85 mm towards 0.51-0.52 mm.

For the rest of the discussion, we will take $p = 0.03$ as the subsampling factor for the non-zero angle raw RF data frames. Figure 4.7 illustrates the effect of subsampling applied to the 16°-angle TYPE-2 raw RF data frame. Figure 4.7 (a) shows the grayscale image of the absolute values of $P_\theta(t,x)$ elements (100% RF data), while Figure 4.7 (b) shows the corresponding image of $P_\theta^*(t,x)$ for $p = 0.03$ (3% RF data). Note that we were able to capture many large-magnitude samples, whose locations were specified in advance by $M_\theta(t,x)$ derived from $S_0^M(k_z,x)$ for $\theta = +16°$. Recall that $S_0^M(k_z,x)$ itself is generated from $M_0(t,x)$. In this work, we obtain $M_0(t,x)$ from the initial zero-angle RF data $P_0(t,x)$ acquired in full: we simply identify the locations of the first $N_{p=0.03}$ largest magnitude samples in $P_0(t,x)$, and then set the corresponding elements in $M_0(t,x)$ to 1 (all other data entries are set equal to 0) [53].

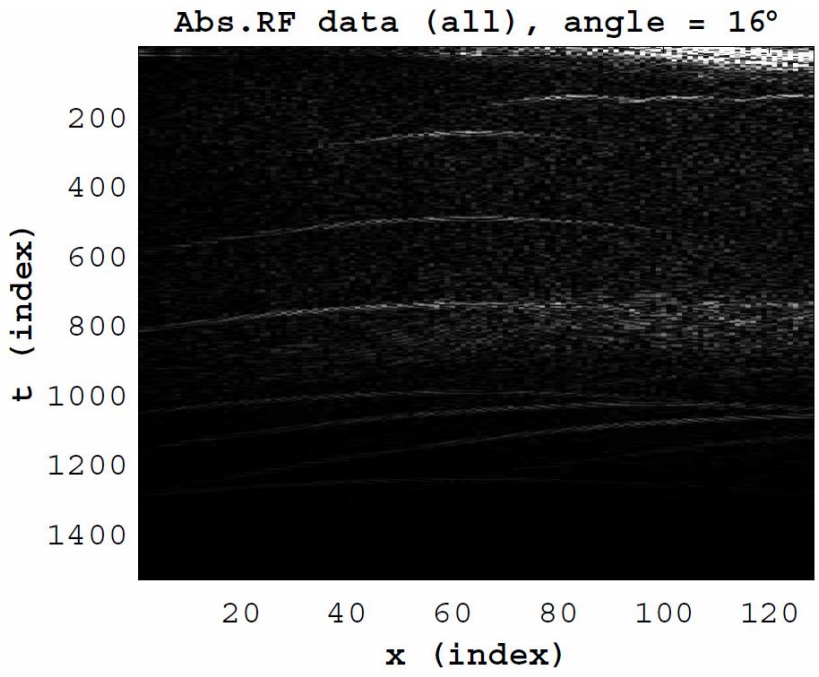

(a)

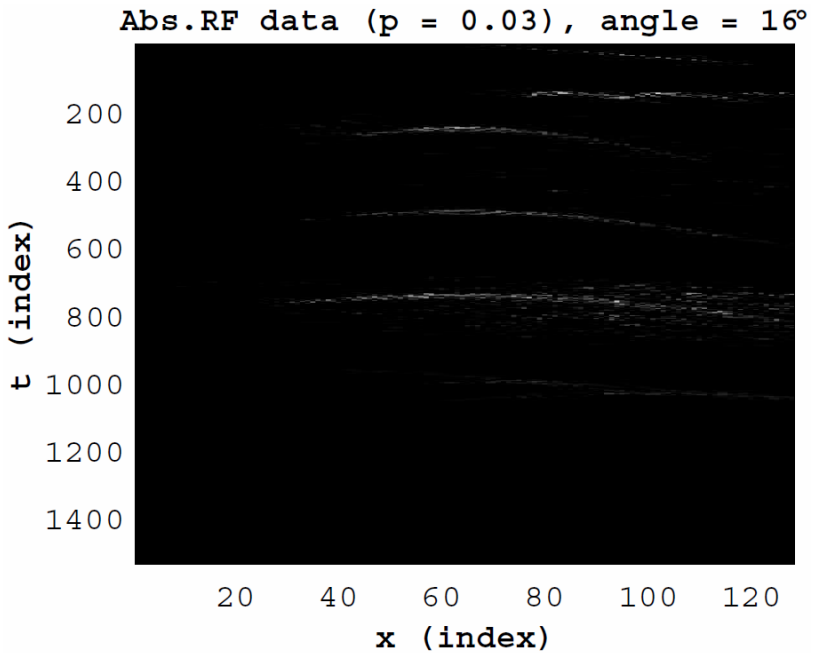

(b)

Figure 4.7: Subsampling illustration: TYPE-2 RF data, $\theta = +16^{\circ}, p = 0.03$ [53].

4.2 Option A

In the 5PW case, we have $N_a - 1 = 4$ non-zero angle raw RF data frames. Since the zero-angle frame is fully acquired, and $p = 0.03$, the overall acquisition data cost we are performing is 20% data attributed to the zero-angle frame plus another 2.4% data of the other 4 non-zero data frames, which would give us an overall savings of 77.6% (i.e. only about 22% of data is used to reconstruct the image). We should note that the derivation of $\widetilde{H}(z, x)$ is performed according to equation (3.8), as we do not acquire additional data from the non-zero angle RF data frames.

Table 4.3 shows the result of our subsampling scheme.

Table 4.3: Image quality indicators for option A

Case	TYPE-1			TYPE-2	
	Top/Bottom CNR (dB)	Axial/Lateral FWHM (mm)	Speckle Test	Axial/Lateral $\overline{\text{FWHM}}$ (mm)	Speckle Test
22% of 5PW	6.1/6.0	0.46/0.64	Pass 4/4	0.47/0.60	Pass 2/2
7% of 25PW	6.9/6.1	0.38/0.75	Pass 4/4	0.44/0.64	Pass 2/2

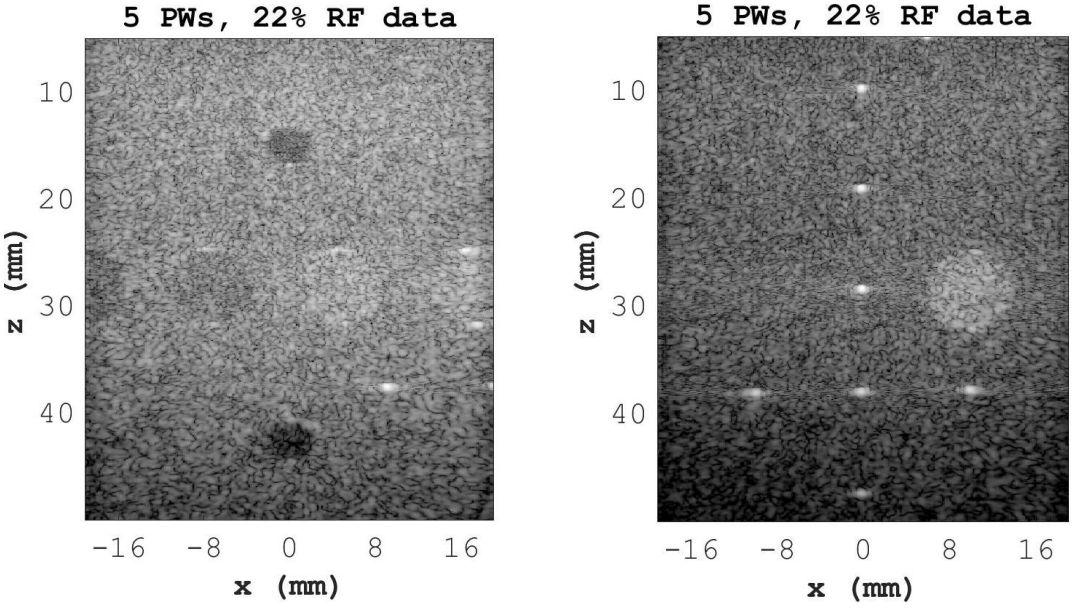

Figure 4.8: Option A, 5PW compounded images using $p = 0.03$.

Table 4.3 and Figure 4.8 confirm the expected lateral FWHM improvement (down to 0.64 mm for TYPE-1 and 0.60 mm for TYPE-2), and we should also mention that both images did pass the Kolmogorov-Smirnov tests for speckle preservation. However, the overall

contrast performance degraded and was not within our expected contrast interval. This discrepancy can be attributed to the fact that our current approach favors large-magnitude samples, thus aiming to capture signals from strong reflectors, such as wire targets (as opposed to anechoic cysts). Formation of the image portions containing weak reflectors is done mostly by $H_0(z,x)$ and $\widetilde{H}(z,x)$. Our current choice of $\widetilde{H}(z,x)$ appears to be inadequate for TYPE-1 images (in terms of the CNR values obtained).

In the 25PW case, we have $N_a - 1 = 24$ non-zero angle raw RF data frames. With $p = 0.03$, the overall savings are equal to 93%. Table 4.3 and Figure 4.9 confirm the expected lateral FWHM improvement (down to 0.75 mm for TYPE-1 and 0.64 mm for TYPE-2), and we should also mention that both images did pass the Kolmogorov-Smirnov tests for speckle preservation. Similar to the case of 5 PWs, the overall contrast performance also degraded here.

In the next sections, we explore how alternative options B, C, D, E, and F for creating the data filler$\widetilde{H}(z,x)$ are affecting the CNR values in question.

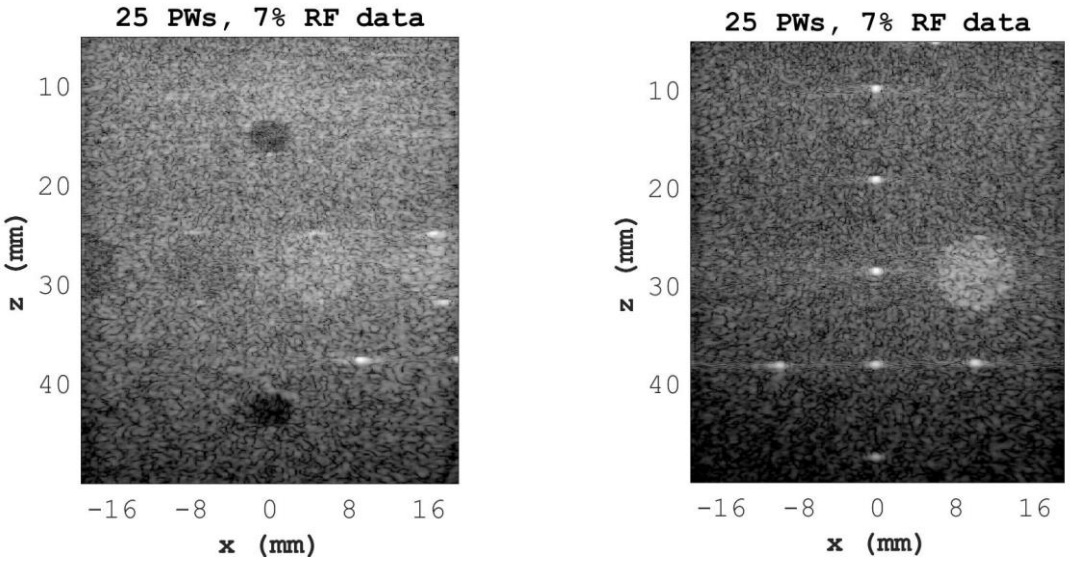

Figure 4.9: Option A, 25PW compounded images using $p = 0.03$.

4.3 Option B

Our regular down-sampling scheme applied to $\bar{P}_\theta{}^*(t,x)$ is done using $S_t = 4$ and $S_x = 2$, which is equivalent to acquiring approximately 12% of $\bar{P}_\theta{}^*(t,x)$ and setting the rest to zero. This results in 32% acquisition cost (68% total savings) for 5PW, and 18% acquisition cost (82% total savings) for 25PW. The target analytic-signal output of the extra acquired data is then obtained and added to $\widetilde{H}(z,x)$, according to equation (3.11). For the 5PW case shown in Figure 4.10, Table 4.4 shows that the contrast of the cyst phantoms is reduced compared to option A results. On the other hand, for the 25PW case shown in Figure 4.11, the CNR values have improved. We expected the contrast to improve (as we are acquiring more raw data), however this expectation was met only in the 25PW case.

As for resolution, Table 4.4 shows that option B is better than option A in terms of the lateral FWHM values; however, option A offers better axial resolution. We should also note that all images passed the speckle test.

Table 4.4: Image quality indicators for option B

Case	TYPE-1			TYPE-2	
	Top/Bottom CNR (dB)	Axial/Lateral FWHM (mm)	Speckle Test	Axial/Lateral $\overline{\text{FWHM}}$ (mm)	Speckle Test
32% of 5PW	5.4/5.6	0.50/0.62	Pass 4/4	0.48/0.57	Pass 2/2
18% of 25PW	7.4/6.8	0.42/0.68	Pass 4/4	0.45/0.60	Pass 2/2

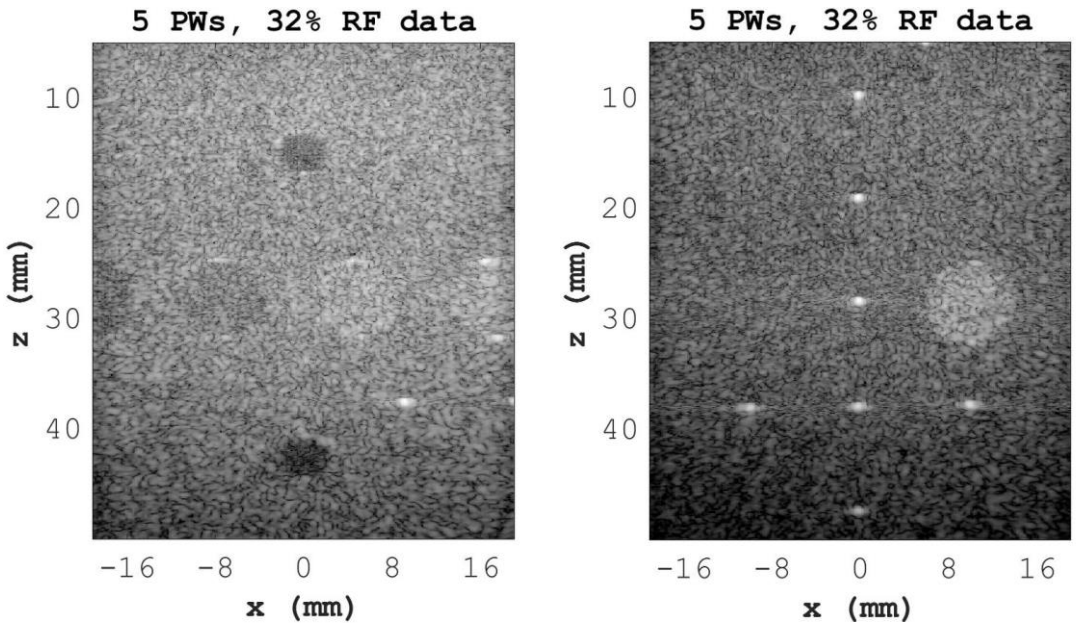

Figure 4.10: Option B, 5PW compounded images using $p = 0.03$ with $S_t = 4$ and $S_x = 2$.

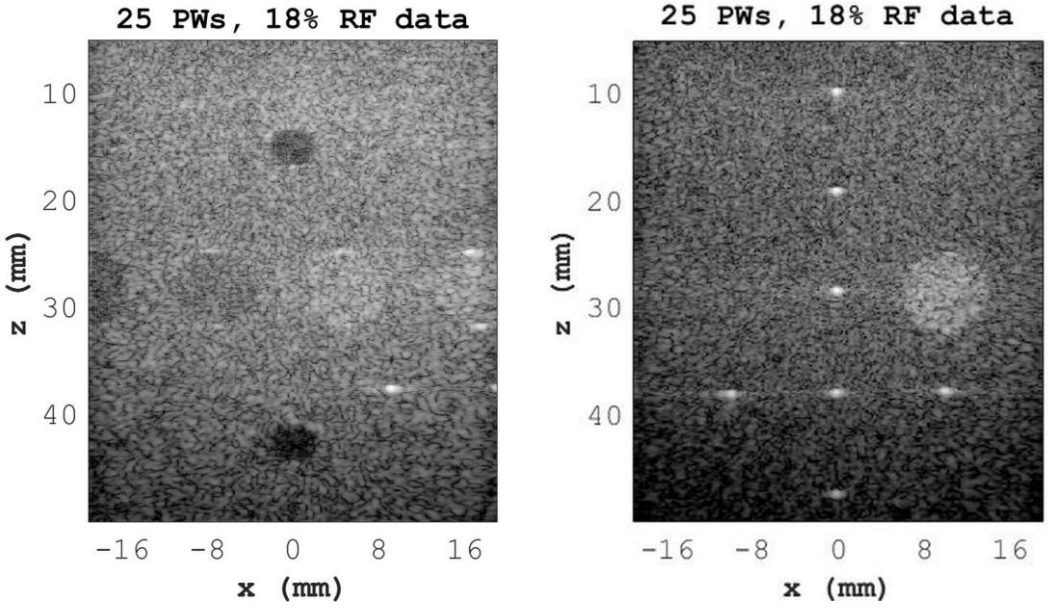

Figure 4.11: Option B, 25PW compounded images using $p = 0.03$ with $S_t = 4$ and $S_x = 2$.

4.4 Option C

Our random subsampling results, shown in Table 4.5 and Figures 4.12 and 4.13, are similar to those obtained using option B. Acquiring 12% of $\bar{P}_\theta{}^*(t,x)$ at random yields an overall acquisition cost of 32% for 5PW and 18% for 25PW. Compared to option A, the cyst contrast is better in the 25PW case (but worse in the 5PW case), and the point resolution is better laterally (while practically the same axially). This choice of $\widetilde{H}(z,x)$ does not offer any significant advantage over option B.

Table 4.5: Image quality indicators for option C

Case	TYPE-1			TYPE-2	
	Top/Bottom CNR (dB)	Axial/Lateral FWHM (mm)	Speckle Test	Axial/Lateral $\overline{\text{FWHM}}$ (mm)	Speckle Test
32% of 5PW	5.3/5.6	0.45/0.60	Pass 4/4	0.46/0.57	Pass 2/2
18% of 25PW	7.2/6.6	0.39/0.72	Pass 4/4	0.44/0.62	Pass 2/2

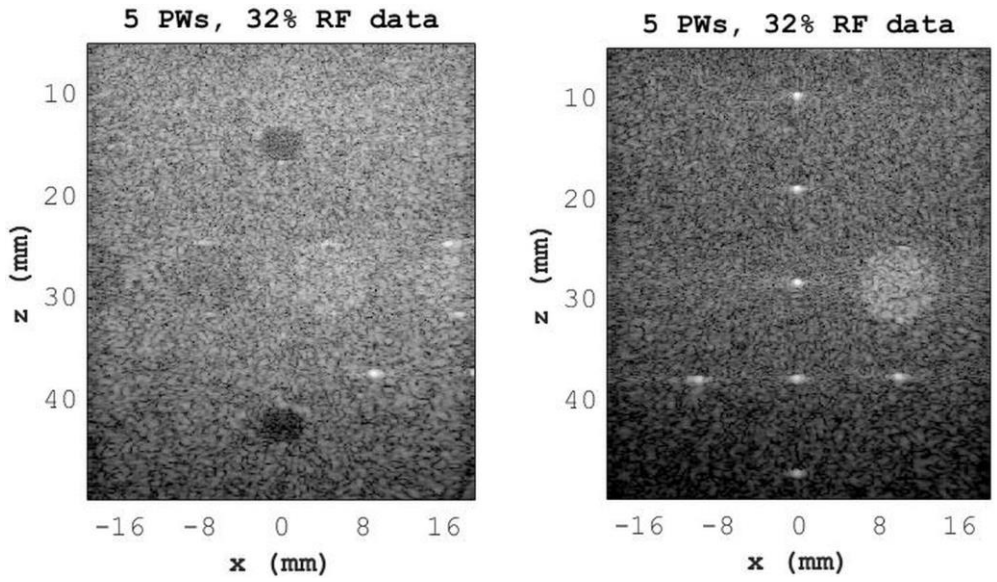

Figure 4.12 Option C, 5PW compounded images using $p = 0.03$ and the random subsampling factor of 12%.

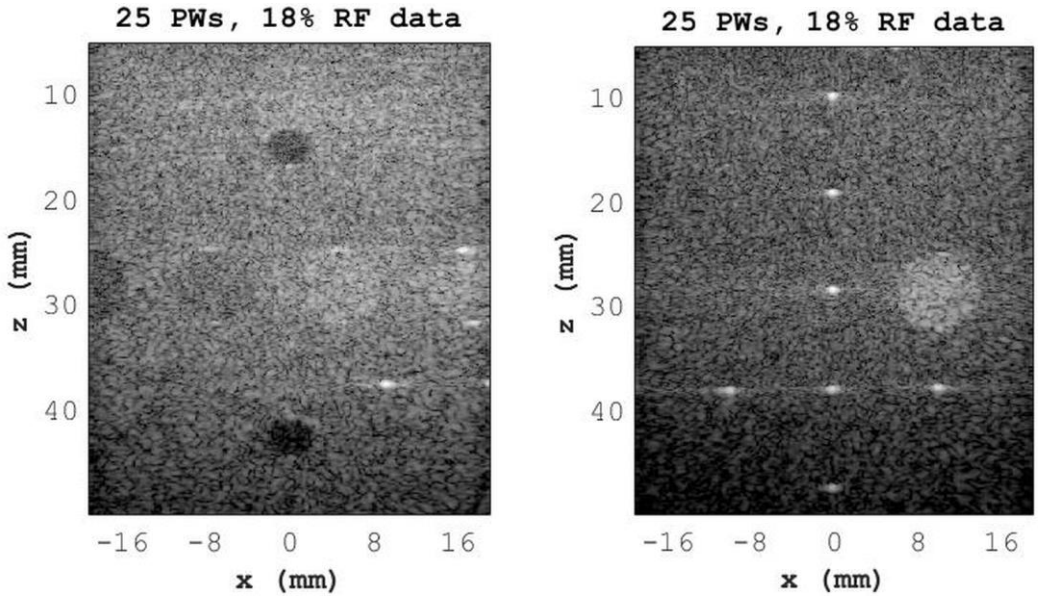

Figure 4.13: Option C, 25PW compounded images using $p = 0.03$ and the random subsampling factor of 12%.

4.5 Option D

The purpose of this option is to attempt sparse recovery after random subsampling. The acquisition cost stays the same as that of option C (i.e., additional 12% of nonzero-angle raw data samples), but the computational cost becomes higher due to sparsity-promoting optimization. In this work, sparse recovery was performed according to the steps described in section 3.3.4 and by applying the parameters shown in Table 4.6.

Table 4.6: Sparse recovery parameters

Parameter	**Values**
Algorithm	l1eq_pd, primal-dual recovery algorithm [46]
Ψ	Discrete Fourier Transform (DFT) matrix
s	0.12
$pdmaxiter$ (number of iterations)	10 (default is 50)
$pdtol$ (duality gap)	0.01 (default is 0.001)

We should note that the decreased number of iterations as well as the value of the duality gap (compared to default numbers) did not affect the image quality, but it did improve the computational speed of the algorithm.

As shown in Table 4.7 and Figures 4.14 and 4.15, our attempt to improve the image quality using sparse recovery was of very limited success. There was some improvement in the CNR values for the top cyst, but the resolution metrics under consideration became slightly worse.

Table 4.7: Image quality indicators for option D

Case	TYPE-1			TYPE-2	
	Top/Bottom CNR (dB)	Axial/Lateral FWHM (mm)	Speckle Test	Axial/Lateral $\overline{\text{FWHM}}$ (mm)	Speckle Test
32% of 5PW	5.9/5.3	0.49/0.62	Pass 4/4	0.48/0.58	Pass 2/2
18% of 25PW	7.8/6.6	0.41/0.68	Pass 4/4	0.45/0.61	Pass 2/2

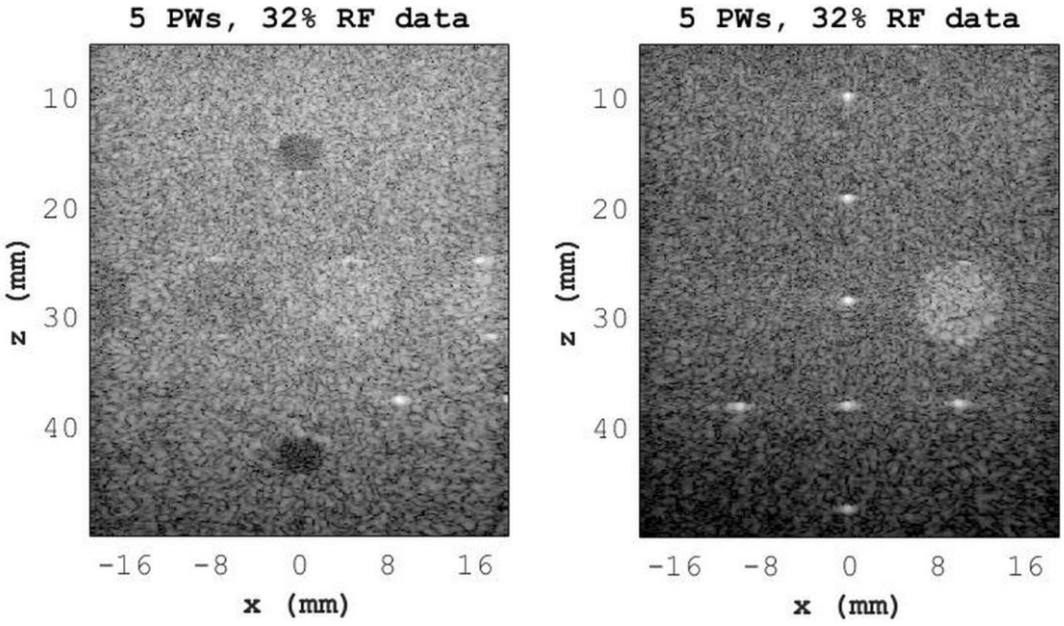

Figure 4.14: Option D, 5PW compounded images using $p = 0.03$ and the random subsampling factor of 12% plus sparse recovery.

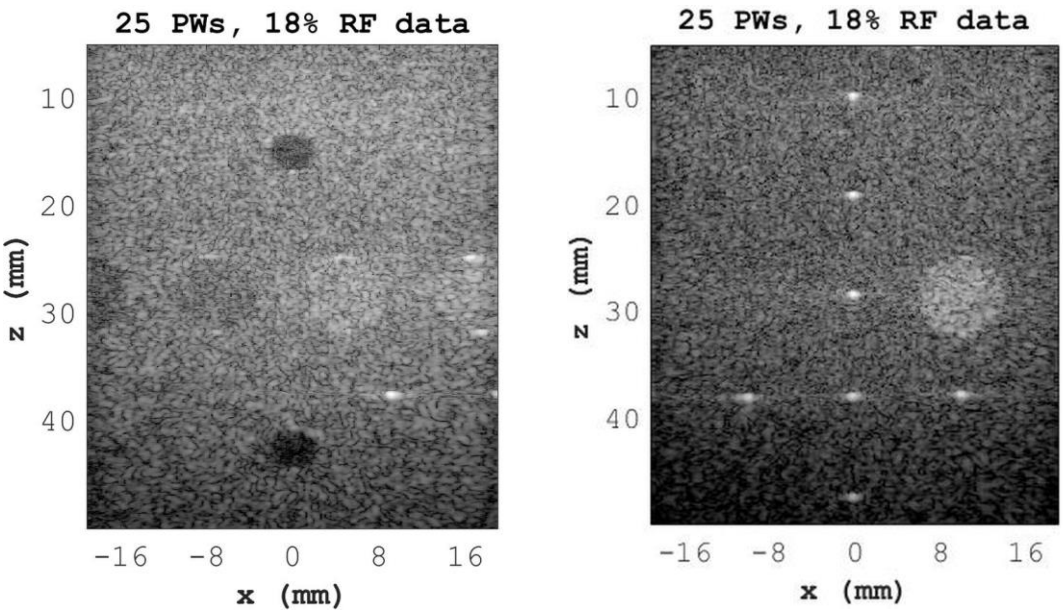

Figure 4.15: Option D, 25PW compounded images using $p = 0.03$ and the random subsampling factor of 12% plus sparse recovery.

4.6 Option E

As described in section 3.3.5, option E does not involve any extra data acquisition to enhance the resulting image quality. The smoothing process detailed in step 2 of paragraph 3.3.5, is done through a median filter of order 5 and with a window size of 3-by-3 pixels, which replaces each element in $absH_0(z,x)$ by the fifth element in the sorted set of neighbors specified by the nonzero elements in matrix window. Next, we normalize $absH_0(z,x)_{smooth}$ by its maximum value, and then we apply our local adaptive thresholding to the resulting matrix to binarize it. In our case, the threshold luminance value is set to 0.99. We should also mention that we apply a max filter to the binarized signal to further dilate it and reduce any leftover artifacts, to finally obtain $H_{mask}\ (z,x)$. Results, shown in Table 4.8 and Figure 4.16, indicate a significant improvement in the bottom cyst phantom contrast for both 5PW and 25PW. However, the top cyst phantom contrast quality

decreases for 25 PW. Compared to option A, FWHM measurements and the acquisition cost are the same. Computational cost for option E is slightly higher due to the additional smoothing and binarizing processes.

Table 4.8: Image quality indicators for option E

Case	TYPE-1			TYPE-2	
	Top/Bottom CNR (dB)	Axial/Lateral FWHM (mm)	Speckle Test	Axial/Lateral $\overline{\text{FWHM}}$ (mm)	Speckle Test
22% of 5PW	7.4/9.4	0.46/0.64	Pass 4/4	0.47/0.60	Pass 2/2
7% of 25PW	5.4/10.8	0.38/0.75	Pass 4/4	0.44/0.63	Pass 2/2

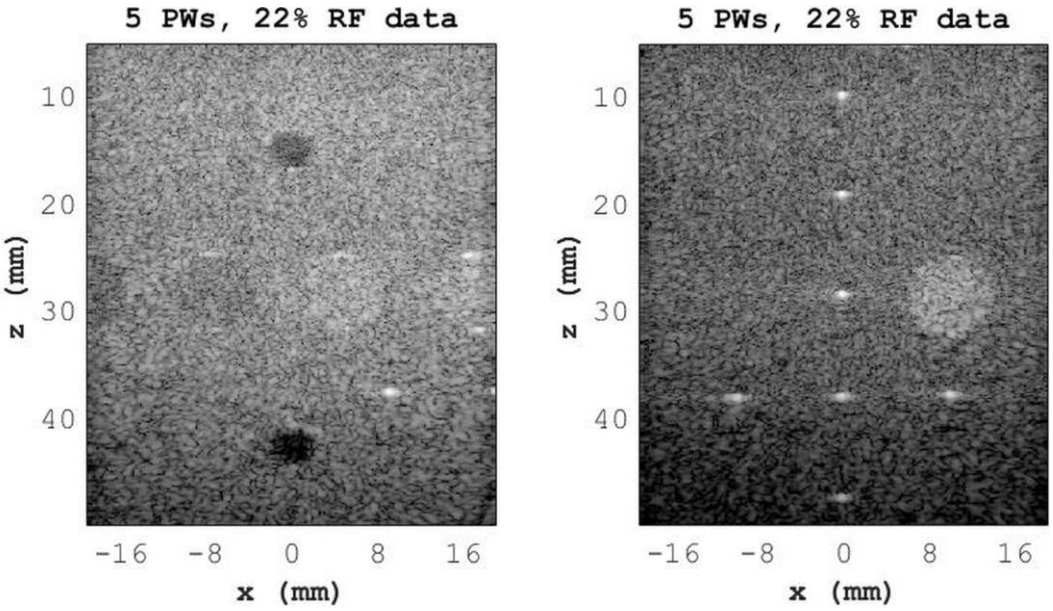

Figure 4.16: Option E, 5PW compounded images using $p = 0.03$ with target output masking.

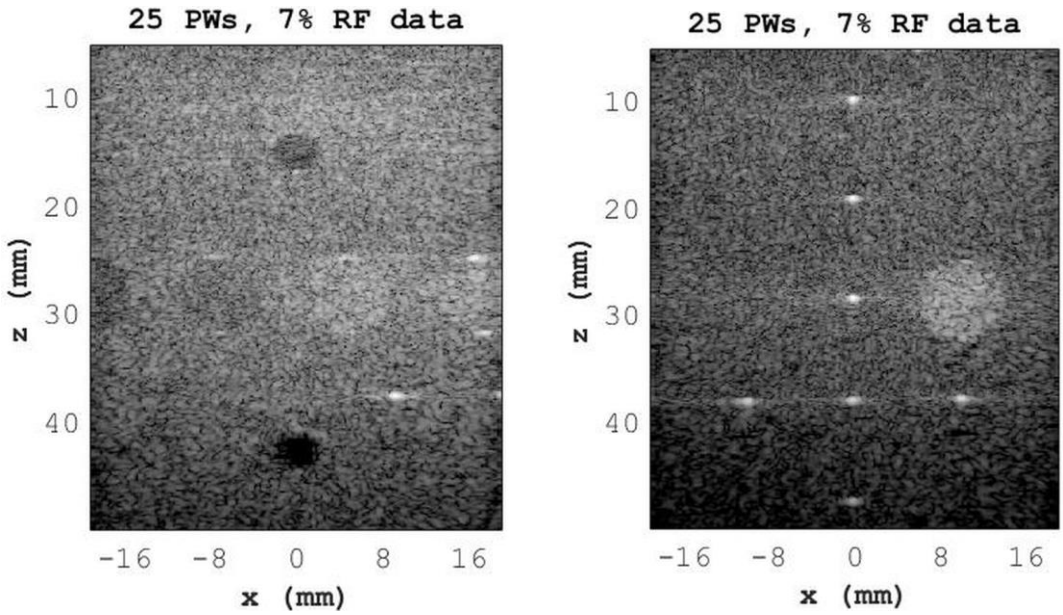

Figure 4.17: Option E, 25PW compounded images using $p = 0.03$ with target output masking.

4.7 Option F

This option follows the same steps as in option E, except that we perform the smoothing process of $absH_0(z,x)$ by applying homomorphic Butterworth filtering instead. We deploy the NSRFilters package from [60] and [49] using a first order Butterworth filter with a cutoff frequency $W_0 = 30$. Once smoothed, $absH_0(z,x)$ undergoes a binarization process (similar to option E) to obtain $H_{mask}\,(z,x)$. We should mention that further dilation (via max filtering done for option E) is not needed here. Table 4.9 along with Figures 4.18 and 4.19 show further improvement to the bottom cyst phantom contrast compared to options A and E. the top cyst phantom contrast saw a slight increase while the FWHM values remained unchanged. We should also note that raw data acquisition cost for option F is equal to that of options A and E, however, computational cost is significantly

higher than both, since we apply direct/inverse Fourier transforms and ln/exp operations when deriving our target output mask.

Table 4.9: Image quality indicators for option F

Case	TYPE-1			TYPE-2	
	Top/Bottom CNR (dB)	Axial/Lateral FWHM (mm)	Speckle Test	Axial/Lateral $\overline{\text{FWHM}}$ (mm)	Speckle Test
22% of 5PW	7.9/10.2	0.46/0.64	Pass 4/4	0.47/0.60	Pass 2/2
7% of 25PW	5.5/12.6	0.38/0.75	Pass 4/4	0.44/0.63	Pass 2/2

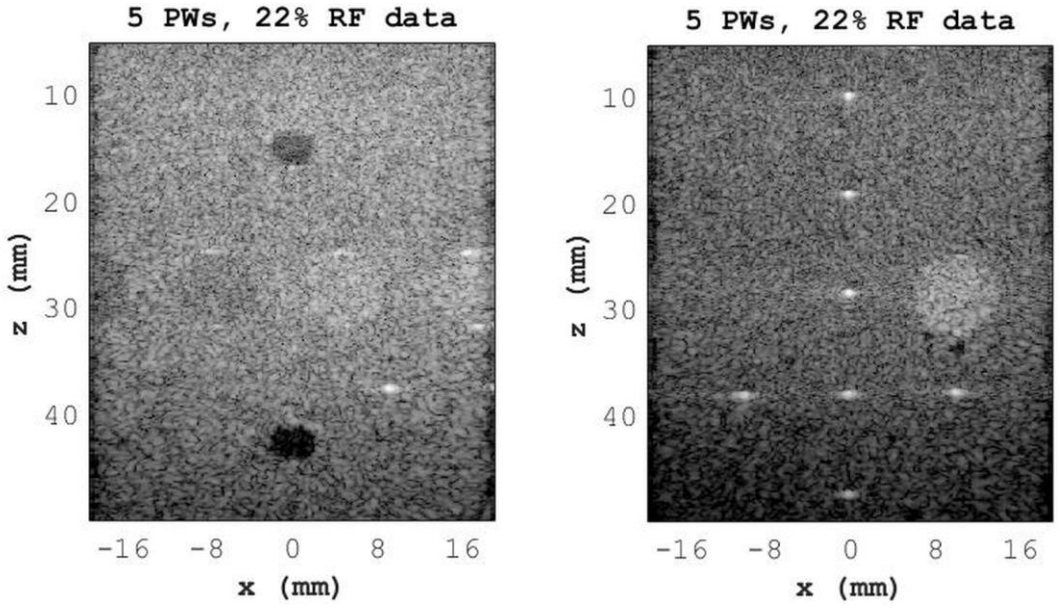

Figure 4.18: Option F, 5PW compounded images using $p = 0.03$ with target output masking.

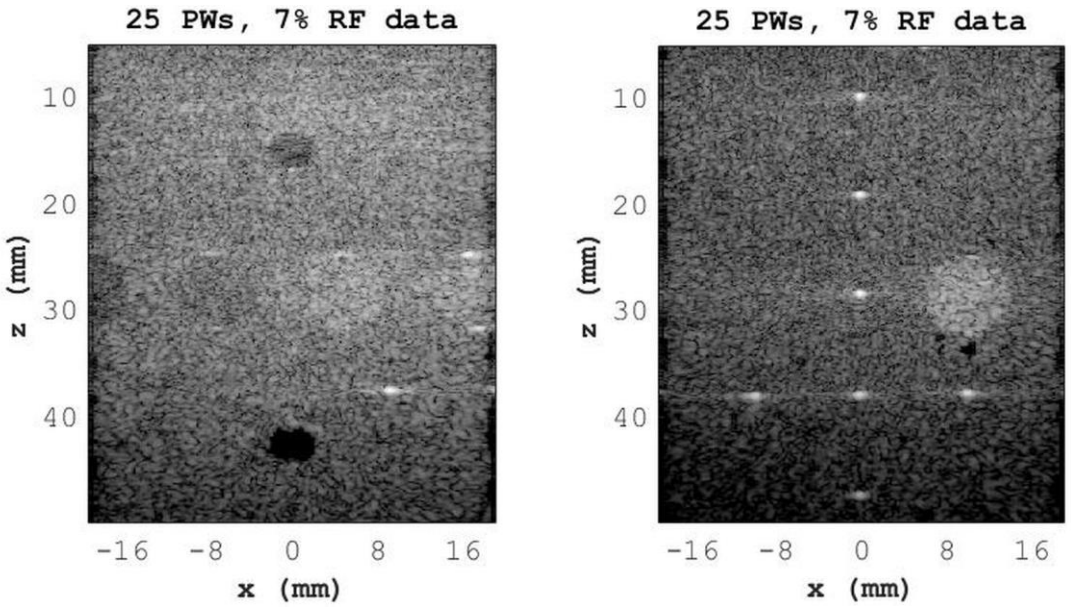

Figure 4.19: Option F, 25PW compounded images using $p = 0.03$ with target output masking.

4.8 Comparative Summary

In this chapter, we will perform an overall comparison of the acquisition and computation cost as well as the performance of each option we previously presented. Table 4.10 summarizes our image quality measurements for these different options.

First, we have options A, E, and F that do not add any extra acquisition cost beyond deterministically acquiring 3% data from $P_\theta(t,x)$ to obtain ${P_\theta}^*(t,x)$, which gives total savings of 78% in the case of 5PWs and 93% for 25PWs. Unlike option A, options E and F entail additional computational cost as they derive a target output mask $H_{mask}\ (z,x)$ to enhance the data filler. In Table 4.10, we can clearly see the effects of using a simple median filter versus using a Homomorphic Butterworth filter: the CNR values have improved for the top cyst and the bottom cyst phantoms in both 5PW and 25PW cases.

Table 4.10: Summary of image quality indicators for all options

Case		Acq. Cost (%)	TYPE-1			TYPE-2	
			Top/Bottom CNR (dB)	Axial/Lateral FWHM (mm)	Speckle Test	Axial/Lateral $\overline{FWHM}$ (mm)	Speckle Test
1PW		100	8.6/6.0	0.48/0.85	Pass 4/4	0.48/0.80	Pass 2/2
5PW		100	8.0/9.5	0.49/0.48	Pass 4/4	0.47/0.44	Pass 2/2
25PW		100	12.6/11.7	0.48/0.52	Pass 4/4	0.49/0.51	Pass 2/2
Option A	5PW	22	6.1/6.0	0.46/0.64	Pass 4/4	0.47/0.60	Pass 2/2
	25PW	7	6.9/6.1	0.38/0.75	Pass 4/4	0.44/0.64	Pass 2/2
Option B	5PW	32	5.4/5.6	0.50/0.62	Pass 4/4	0.48/0.57	Pass 2/2
	25PW	18	7.4/6.8	0.42/0.68	Pass 4/4	0.45/0.60	Pass 2/2
Option C	5PW	32	5.3/5.6	0.45/0.60	Pass 4/4	0.46/0.57	Pass 2/2
	25PW	18	7.2/6.6	0.39/0.72	Pass 4/4	0.44/0.62	Pass 2/2
Option D	5PW	32	5.9/5.3	0.49/0.62	Pass 4/4	0.48/0.58	Pass 2/2
	25PW	18	7.8/6.6	0.41/0.68	Pass 4/4	0.45/0.61	Pass 2/2
Option E	5PW	22	7.4/9.4	0.46/0.64	Pass 4/4	0.47/0.60	Pass 2/2
	25PW	7	5.4/10.8	0.38/0.75	Pass 4/4	0.44/0.63	Pass 2/2
Option F	5PW	22	7.9/10.2	0.46/0.64	Pass 4/4	0.47/0.60	Pass 2/2
	25PW	7	5.5/12.6	0.38/0.75	Pass 4/4	0.44/0.63	Pass 2/2

Second, we have options B, C, and D that acquire an additional 12% of raw data from $\bar{P}_\theta{}^*(t,x)$, which gives total savings of 68% for 5PWs and 82% for 25 PWs. While option B acquires the additional 12% data regularly, option C and D acquire the same amount of data randomly. Implementing options B and C is less costly than option D. For example, in our computational experiments option D takes approximately 50 times more time than option C to generate the final images in the 5PW case.

As for the image quality of each option, we are to compare the following: the near field contrast (top cyst) and the far field contrast (bottom cyst) for TYPE-1 images, as well as lateral and axial resolution for TYPE-1 and TYPE-2 images, for both 5PW and 25PW. For the near field contrast, option F has the best CNR of 7.90 dB (about 30% improvement compared to option A) in the case of 5PW, while option D has the best CNR of 7.80 dB (about 13% improvement compared to option A) in the case of 25PW. Note that option D does not offer significant improvements compared to much faster option C producing near-field CNR of 7.2 dB (given that both options add the same amount of extra raw data at random). For the far field contrast, option F has the best CNR of 10.20 dB (70% improvement compared to option A) for 5PW and 12.6 dB (107% improvement compared to option A) for 25 PW. Option E has produced the second-best CNR of 9.40 dB for 5PW and 10.8 dB for 25PW. Note that option F has produced better far-field CNR values than both 5PW FA and 25PW FA cases.

For TYPE-1 images, option C has the best axial FWHM of 0.45 mm for 5PW, while options A, E, and F share the best axial FWHM of 0.38 mm for 25PW. Similarly, for TYPE-2 images, option C has the best result with 0.46 mm for 5PW, while options A, E, and F for 25PW share the best axial FWHM of 0.44 mm. These results are in fact better than those

obtained with FA 5PW and FA 25PW, which indicates the benefit of our deterministic subsampling scheme in both types of our images. For TYPE-1 lateral images, option C also has the best lateral FWHM of 0.60 mm for 5PW, and options B and D share the best lateral FWHM of 0.68 mm for 25PW. For TYPE-2 images, option B has the best lateral FWHM of 0.57 mm (shared with option C) for 5PW, and 0.60 mm for 25PW.

To sum up, in the 5PW case, option F's near-field CNR of 7.90 dB is very close to FA's 8.00 dB, which shows that with only 22% acquired raw data, it is possible to reach almost the same near-filed contrast values as in the full-acquisition case. However, no option managed to obtain a near-field CNR value close to FA's 12.60 dB for 25PW. As for far field contrast, we should note that option F results are better in comparison to the full-acquisition case (10.2 vs 9.5 dB for 5PW, and 12.6 vs 11.7 dB for 25PW). In terms of axial resolution, option C has better FWHM than FA for 5PW (0.45 vs 0.49 mm for TYPE-1 and 0.46 vs 0.47 mm for TYPE-2), while options A, E, and F have better FWHM than FA for 25PW (0.38 vs 0.48 mm for TYPE-1 and 0.44 vs 0.49 mm for TYPE-2). In terms of lateral resolution, option C improves FWHM, in comparison to FA 1PW, from 0.85 mm to 0.60 mm for TYPE-1 5PW, and from 0.80 mm to 0.57 mm for TYPE-2 5PW. However, these results are not close to FWHM of 0.48 mm/0.44 mm for TYPE1/TYPE2 for FA 5PW. For 25PW, option D improves FWHM, in comparison to FA 1PW, from 0.85 mm to 0.68 mm for TYPE-1, and from 0.80 mm to 0.61 mm for TYPE-2, but it is still far from FA 25PW FWHM of 0.52 and 0.51 mm for TYPE-1 and TYPE-2, respectively. Finally, we should note that, in the 25PW case, options B, C, and D, having the acquisition cost of approximately 18%, did not provide expected contrast improvements. In this case, it is

better to perform full acquisition of 5PW at 20% cost (out of 25 PW), which yields better contrast and lateral resolution, while sacrificing axial resolution.

Next, we put together visually and compare our TYPE-1 and TYPE-2 images in their entirety. We have organized them into the following four groups: 5PW with no extra data, 5PW with extra data, 25PW with no extra data, and 25PW with extra data. Recall that “no extra data” refers to options A, E, and F, while “extra data” refers to options B, C, and D.

Figure 4.20 shows the 22%-5PW images for options A, E, and F, next to the FA 1PW and FA 5PW images. All options managed to capture all the structures present in the full-acquisition images. As expected, the point phantoms in our subsampled images appear slightly sharper than in the 1PW case, but not as focused as in the FA 5PW case. As for the cyst phantoms, the top one has slightly poorer visibility than the bottom one in all cases. Options E and F produce the bottom cyst section that is visually competitive with the FA 5PW case, which is supported by the numerical results in Table 4.10.

Similar observations can be made in Figure 4.21 for 25PW. In comparison to 1PW, the point phantoms are better focused, but they also show brighter sidelobes with respect to the background. This is likely due to the fact that our coherent compounding involves 24 frames that emphasize only strong reflectors. For the same reason, one can observe that the top cyst (a weak reflector) is not well-imaged. The bottom cyst, however, has better visibility for options E and F due to filtering.

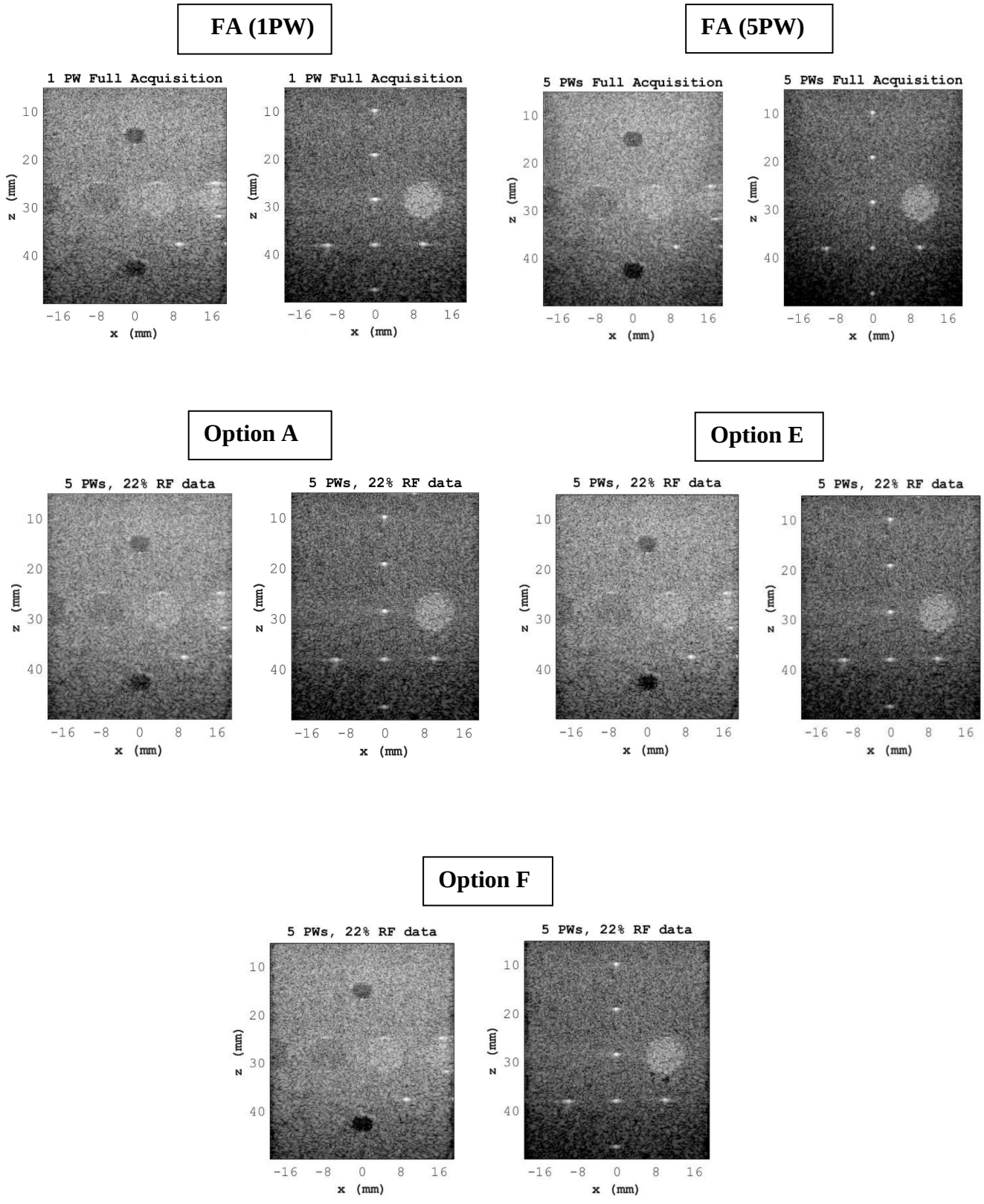

Figure 4.20: No extra data options – 5PW.

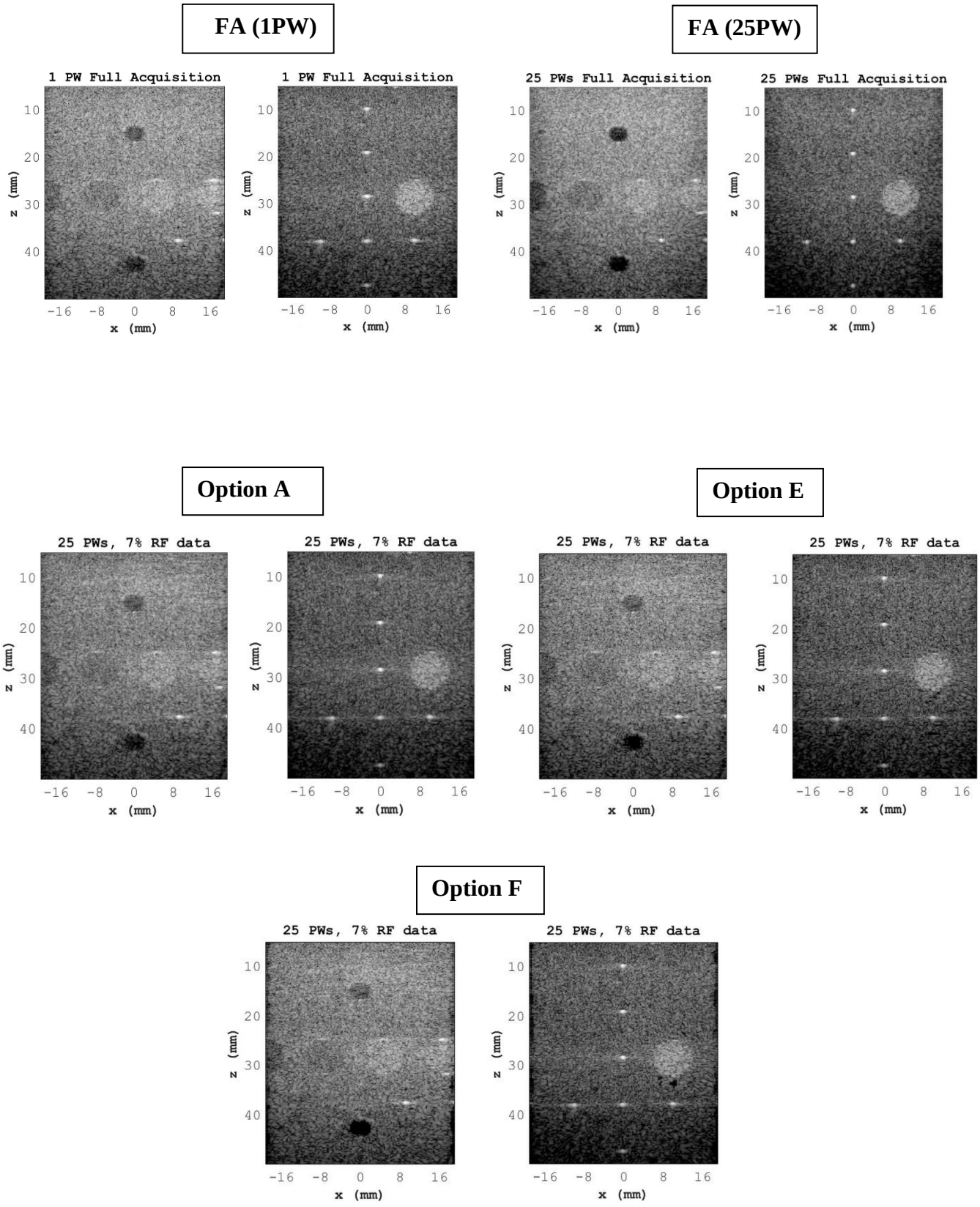

Figure 4.21: No extra data options – 25PW.

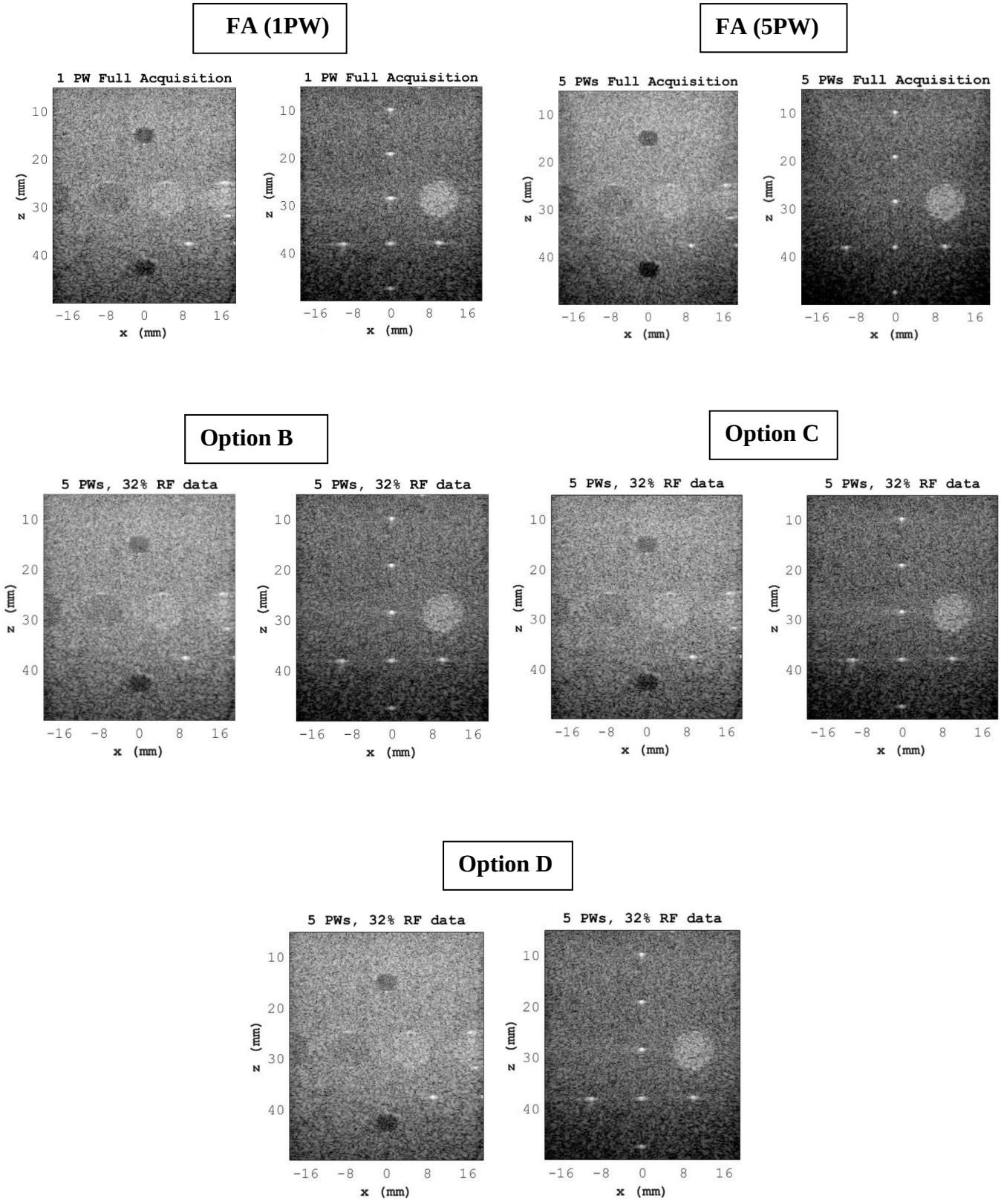

Figure 4.22: Extra data options – 5PW.

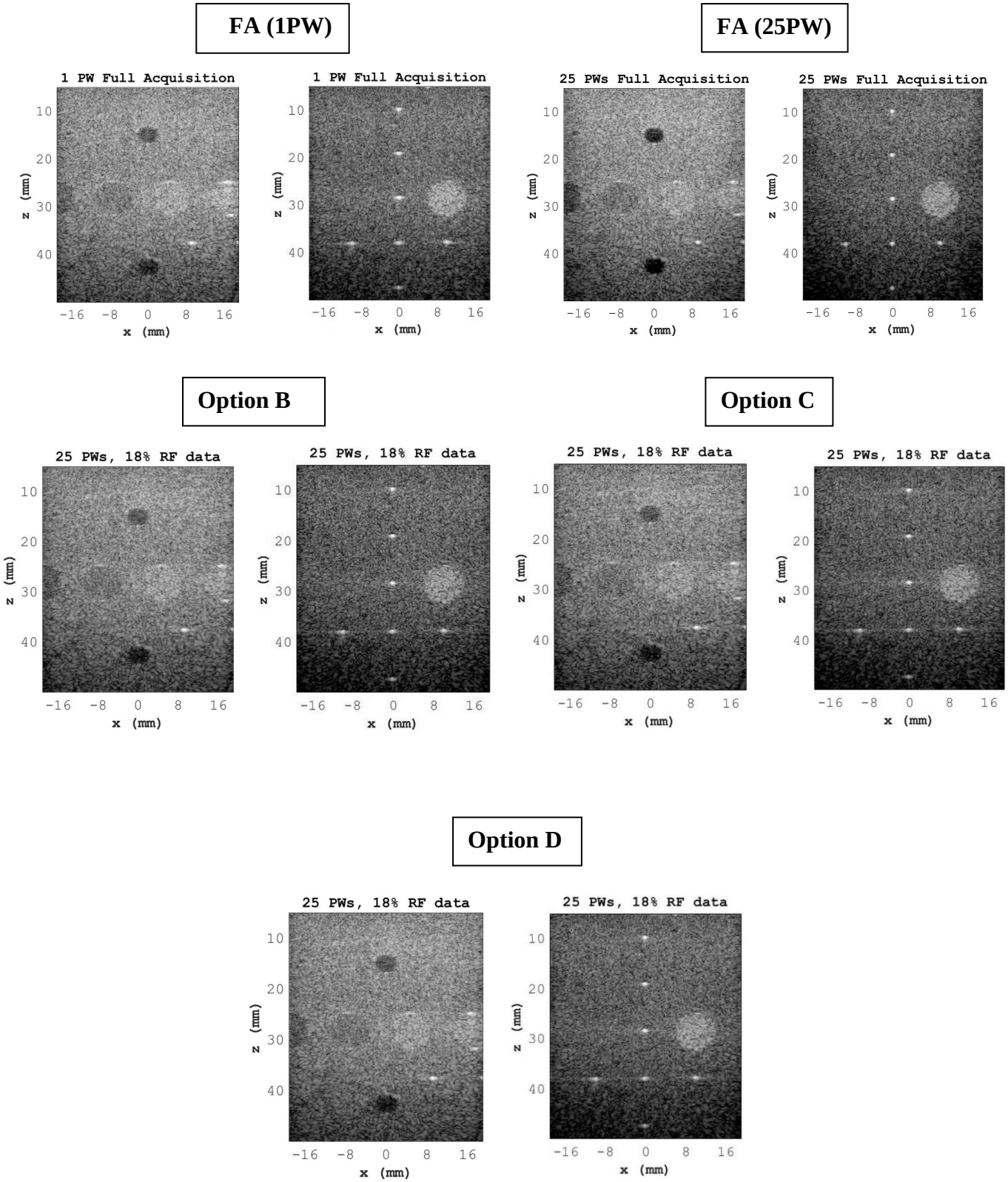

Figure 4.23: Extra data options – 25PW.

Figures 4.22 and 4.23 show that acquiring extra data (with respect to 1PW or option A) is beneficial only for 25PW, which is also supported by the numerical results in Table 4.10. Since the acquisition cost of 18% (options B, C, and D for 25PW) is close to 20%, we can instead fully acquire 5 PWs (i.e., 20% of 25 PWs), which is equivalent to our FA 5PW case. The latter yields better images, both visually and numerically.

Finally, we should note that Table 4.10 shows no clear emerging data pattern. For example, even in the FA case, one can observe that using 5PW vs. 1PW has both positive and negative ramifications (namely, better lateral FHWM and worse near-field CNR values). On the other hand, using 25PW vs. 5PW yields worse lateral FWHM and better near-field CNR values. These inconsistencies give rise to more questions than answers as to why the numerical image quality indicators exhibit such a behavior. Further research is needed to adequately address this issue in the future.

Chapter 5: Conclusion and Future Work

In this chapter, we will summarize the work done in our thesis and suggest potential future research directions.

5.1 Conclusion

This thesis takes advantage of the zero-angle data frame to derive a deterministic subsampling mask for any nonzero-angle data frame acquisition. Such masks are created by using angle-corrected modified Stolt's migration, applied in reverse to the Fourier-domain representation of the reference mask obtained form the zero-angle data. This work also presents several options for creating a data filler with the goal of mitigating the negative impact of subsampling. We have evaluated our scheme based on the two types of B-mode images: near and far field anechoic cyst phantoms (TYPE-1) used for CNR measurements, and seven-point phantoms (TYPE-2) used for axial/lateral FWHM measurements. These images were reconstructed from subsampled RF channel data in the 5PW and 25PW acquisition.

Notably, option F (homomorphic post-filtering) achieved better far field contrast than FA 5PW and FA 25 PW, while offering 77% and 93% savings respectively (TYPE-1 images). Option C (extra 12% randomly sampled data) yielded better axial resolution values compared to FA 5PW, while all options A-F managed to get better axial resolution values than those of FA 25PW (TYPE-2 images). As for near field contrast and lateral resolution, none of our options came close to FA cases, although they generated visually acceptable results overall. Option D, which involved expensive sparsity-promoting optimization in the Fourier domain, produced similar-quality images as those of option C; both have the same

acquisition cost, the latter is much cheaper computationally (no sparse recovery is attempted). Therefore, option D in its current form is not suitable for image quality enhancement. In the case of 25PW, we recommend taking FA 5PW at 20% acquisition cost (with respect to FA 25PW), instead of using options B, C, and D at 18% acquisition cost.

5.2 Future Work

To enhance the final image quality with the same data savings presented in this work, we suggest the following:

- An alternative sampling scheme, e.g., a sampling mask derived from zero-angle B-mode data ROI instead of zero-angle raw RF data ROI (our current approach is to pick strong reflections);

- Alternative filtering techniques applied to the data matrices before, during, and after migration (such as bandpass pre-filtering, trapezoidal filtering, wavelet post-filtering, etc.);

- A deep learning framework to improve our data filler or to avoid nonzero-angle frame acquisitions altogether (e.g., a deep neural network can be used to either fill in missing raw RF data samples before migration, or serve as a nonlinear post-filter after migration).

Bibliography

[1] J. Powers and F. Kremkau, “Medical ultrasound systems”, Interface Focus 1.4 (2011): 477–489.

[2] R. Cootney, “Ultrasound imaging: Principles and applications in rodent research”, ILAR Journal, 42.3 (2001): 233–247.

[3] A. Gronningsaeter, G. Unsgard, S. Ommedal, and B. A. J. Angelsen, “Ultrasound-guided neurosurgery: a feasibility study in the 3-30 MHz frequency range”, British Journal of Neurosurgery, 10.2 (1996): 161–168.

[4] F. Foster, C. J. Pavlin, K. A. Harasiewicz, D. A. Christopher, and D. H. Turnbull, “Advances in ultrasound biomicroscopy”, Ultrasound in Medicine and Biology 26.1 (2000): 1–27.

[5] D. H. Turnbull, J. A. Ramsay, G. S. Shivji, T. S. Bloomfield, L. From, D. N. Sauder, and F. S. Foster, “Ultrasound backscatter microscope analysis of mouse melanoma progression”, Ultrasound in Medicine and Biology 22.7 (1996): 845–853.

[6] C. R. Merritt, “Physics of ultrasound”, in: C. M. Rumack, S. R. Wilson, J. W. Charboneau, eds. *Diagnostic Ultrasound*. MO: Mosby, (1998): 3–55.

[7] M. Ali, D. Magee, and U. Dasgupta, “Signal processing overview of ultrasound systems for medical imaging”, SPRAB12, Texas Instruments, TX (2008).

[8] H. A. Akbar and D. Rakhmatov, “Efficient angle selection for coherent plane wave compounding”, Proc. 2019 IEEE International Ultrasonics Symposium (IUS), 6-9 October 2019, Glasgow, UK: 2355–2357.

[9] J. Kirkhorn, “Introduction to IQ-demodulation of RF-data”, Technical Report, Norwegian University of Science and Technology, Trondheim, Norway (1999). http://folk.ntnu.no/htorp/Undervisning/TTK10/IQdemodulation.pdf

[10] R. Cobbold, *Foundations of Biomedical Ultrasound*, NY: Oxford University Press, (2007): 420–445.

[11] M. Tanter and M. Fink, “Ultrafast imaging in biomedical ultrasound”, IEEE Transactions on Ultrasonics, Ferroelectrics, and Frequency control 61.1 (2014): 102–119.

[12] A. Ng, J. Swanevelder, “Resolution in ultrasound imaging”, Continuing Education in Anaesthesia Critical Care & Pain, 11.5 (2011): 186–192.

[13] https://www.echocardiographer.org/Echo%20Physics/Axial-and-Lateral Resolution.jpg

[14] W. F. Armstrong, “Physics and instrumentation”, *Feigenbaum's Echocardiography*, PA: Lippincott Williams & Wilkins (2010): 9–38.

[15] J. A. Jensen, “Medical ultrasound imaging”, Progress in Biophysics and Molecular Biology, 93 (2007):153–165.

[16] J. A. Jensen: “Linear description of ultrasound imaging systems”, Notes for the International Summer School on Advanced Ultrasound Imaging, Technical University of Denmark (1999).

[17] M. V. Wijk and J. Thijssen, “Performance testing of medical ultrasound equipment: Fundamental vs. harmonic mode”, Ultrasonics, 40. 1-8 (2002): 585–591.

[18] H. Liebgott, A. Rodriguez-Molares, F. Cervenansky, J. Jensen, and O. Bernard, “Plane-wave imaging challenge in medical ultrasound”, Proc. 2016 IEEE International Ultrasonics Symposium (IUS), 18-21 September 2016, Tours, France: 1–4.

[19] G. Montaldo, M. Tanter, J. Bercoff, N. Benech, and M. Fink, “Coherent plane-wave compounding for very high frame rate ultrasonography and transient elastography”, IEEE Transactions on Ultrasonics, Ferroelectrics, and Frequency Control, 56.3 (2009): 489–506.

[20] C. Papadacci, M. Pernot, M. Couade, M. Fink, and M. Tanter, “High contrast ultrafast imaging of the heart”, IEEE Transactions on Ultrasonics, Ferroelectrics, and Frequency Control, 61.2 (2014): 288–301.

[21] R. E. Carrillo, A. Besson, M. Zhang, D. Friboulet, Y. Wiaux, J.P Thiran, and O. Bernard, “A sparse regularization approach for ultrafast ultrasound imaging”, Proc. 2015 IEEE International Ultrasonics Symposium (IUS), 21-24 October 2015, Taipei, Taiwan: 1–4.

[22] J. Y. Lu, “2D and 3D High Frame Rate Imaging with Limited Diffraction Beams”, IEEE Transactions on Ultrasonics, Ferroelectrics, and Frequency Control, 44.4 (1997): 839–856.

[23] D. Garcia, L. L. Tarnec, S. Muth, E. Montagnon, J. Poree, and G. Cloutier, “Stolt’s *f-k* migration for plane wave ultrasound imaging”, IEEE Transactions on Ultrasonics, Ferroelectrics, and Frequency Control, 60.9 (2013): 1853–1867.

[24] O. Bernard, M. Zhang, F. Varray, P. Gueth, J.-P. Thiran, H. Liebgott, and D. Friboulet, “Ultrasound Fourier slice imaging: a novel approach for ultrafast imaging technique”, in Proc. 2014 IEEE International Ultrasonics Symposium (IUS), 3-6 September 2014, Chicago, IL: 1-4.

[25] J. F. Claerbout, *Imaging the Earth’s Interior*, Vol. 1. Oxford: Blackwell Science, 1985: http://sepwww.stanford.edu/sep/prof/iei/toc_html/.

[26] R. H Stolt, “Migration by Fourier transform”, Geophysics, 43.1 (1978): 23–48.

[27] G. F. Margrave, “Numerical Methods of Exploration Seismology”, CREWES Educational Resources (2003).

[28] J. W. Goodman, *Introduction to Fourier Optics*, CO: Roberts and Company Publishers (2005).

[29] D. D. Liu and R. C. Waag, “Propagation and backpropagation for ultrasonic wavefront design”, IEEE Transactions on Ultrasonics, Ferroelectrics, and Frequency Control, 44.1 (1997): 1–13.

[30] M. Albulayli and D. Rakhmatov, “Fourier-Domain depth migration for planewave ultrasound imaging”, IEEE Transactions on Ultrasonics, Ferroelectrics, and Frequency Control, 65.8 (2018): 1321–1333.

[31] R. Cohen, Y. Sde-Chen, T. Chernyakova, C. Fraschini, J. Bercoff, and Y. C Eldar, “Fourier domain beamforming for coherent plane-wave compounding”, Proc. 2015 IEEE International Ultrasonics Symposium (IUS), 21-24 October 2015, Taipei, Taiwan: 1-4. [32]

N. Wagner, Y. C Eldar, and Z. Friedman, “Compressed beamforming in ultrasound imaging”, IEEE Transactions on Signal Processing 60.9 (2012): 4643–4657.

[33] T. Chernyakova and Y. C Eldar, “Fourier-domain beamforming: the path to compressed ultrasound imaging”, IEEE Transactions on Ultrasonics, Ferroelectrics, and Frequency Control, 61.8 (2014): 1252–1267.

[34] C. Quinsac, A. Basarab, and D. Kouamé, “Frequency domain compressive sampling for ultrasound imaging”, Advances in Acoustics and Vibration (2012): 1–16.

[35] Z. Chen, A. Basarab, and D. Kouamé, “Compressive deconvolution in medical ultrasound imaging”, IEEE Transactions on Medical Imaging 35.3 (2015): 728–737.

[36] A. Besson, M. Zhang, F. Varray, H. Liebgott, D. Friboulet, Y. Wiaux, J.P Thiran, R.E Carrillo, and O. Bernard, “A sparse reconstruction framework for Fourier-based plane-wave imaging”, IEEE Transactions on Ultrasonics, Ferroelectrics, and Frequency Control 63.12 (2016): 2092–2106.

[37] S. Khan, J. Huh, and J.C Ye, “Universal Deep Beamformer for Variable Rate Ultrasound Imaging”, arXiv preprint arXiv:1901.01706 (2019).

[38] R. J Van Sloun, R. Cohen, and Y.C Eldar, “Deep learning in ultrasound imaging”, Proceedings of the IEEE, 108(1) (2019): 11–29

[39] S. Khan, J. Huh, and J.C Ye, “Adaptive and Compressive Beamforming using Deep Learning for Medical Ultrasound”, arXiv preprint arXiv:1907.10257 (2019).

[40] H. Liebgott, R. Prost, and D. Friboulet, “Pre-beamformed RF signal reconstruction in medical ultrasound using compressive sensing”, Ultrasonics 53.2 (2013): 525–533.

[41] E. J. Candès, J. Romberg, T. Tao, Robust uncertainty principles: “Exact signal reconstruction from highly incomplete frequency information”, IEEE Transactions on Information Theory 52 (2006): 489–509.

[42] E. J. Candès, “The restricted isometry property and its implications for compressed sensing”, Compte Rendus de l’Academie des Sciences, 346 (2008): 589–592.

[43] E. Candès and J. Romberg, “Sparsity and incoherence in compressive sampling”, Inverse Problems, 23.3 (2007): 969.

[44] J. Cheng and J. Lu, “Extended high-frame rate imaging method with limited-diffraction beams”, IEEE Transactions on Ultrasonics, Ferroelectrics, and Frequency Control, 53.5 (2006): 880-899.

[45] R. Tur, Y. Eldar, Z. Friedman, “Innovation rate sampling of pulse streams with application to ultrasound imaging,” IEEE Transactions on Signal Processing, 59.4 (2011): 1827-1842.

[46] L1-magic, Justin Romberg, https://jrom.ece.gatech.edu/index-8/

[47] CREATIS, “Plane-wave Imaging Challenge in Medical UltraSound (PICMUS): Algorithm Evaluation Framework”. [Online]. Available: https://www.creatis.insa-lyon.fr/EvaluationPlatform/picmus/

[48] Y. Chen, S.L Broschat, and P.J. Flynn, “Phase insensitive homomorphic image processing for speckle reduction”, Ultrasonic Imaging 18.2 (1996): 122-139.

[49] J. L. Mateo and A. Fernández-Caballero, “Finding out general tendencies in speckle noise reduction in ultrasound images”, Expert Systems with Applications, 36.4 (2009): 7786–7797.

[50] C. Schretter, S. Bundervoet, D. Blinder, A. Dooms, J. D’hooge, and P. Schelkens, “Ultrasound imaging from sparse RF samples using system point spread functions”, IEEE Transactions on Ultrasonics, Ferroelectrics, and Frequency Control, 65.3 (2017): 316–326.

[51] A. Besson, D. Perdios, F. Martinez, Z. Chen, R.E Carrillo, M. Arditi, Y. Wiaux, and J-P. Thiran, “Ultrafast ultrasound imaging as an inverse problem : matrix-free sparse image reconstruction”, IEEE Transactions on Ultrasonics, Ferroelectrics, and Frequency Control, 65.3 (2017) : 339–355.

[52] E. Ozkan, V. Vishnevsky, and O. Goksel, “Inverse problem of ultrasound beamforming with sparsity constraints and regularization”, IEEE transactions on Ultrasonics, Ferroelectrics, and Frequency Control, 65.3 (2017): 356–365.

[53] H. Marzougui and D. Rakhmatov, “Data-driven sensor array subsampling for plane-wave ultrasound imaging”, Proc. 2019 IEEE International Ultrasonics Symposium (IUS), 6-9 October 2019, Glasgow, UK: 2337-2340.

[54] T. Szabo, *Diagnostic Ultrasound Imaging: Inside Out*. MA: Elsevier (2014): p.25.

[55] D. D. Liu, and T. L. Ji, “Plane wave image formation in spatial-temporal frequency domain”, Proc. 2016 IEEE International Ultrasonics Symposium (IUS), 18-21 September 2016, Tours, France: 1-4.

[56] N. Wagner, Y. C. Eldar, A. Feuer, G. Danin, and Z. Friedman, “Xampling in ultrasound imaging”, Medical Imaging 2011: Ultrasonic Imaging, Tomography, and Therapy. International Society for Optics and Photonics, 7968 (2011).

[57] M. A. Davenport, M. F. Duarte, Y. C. Eldar, and G. Kutyniok, “Introduction to compressed sensing”, in *Compressed Sensing: Theory and Applications*, Y. C. Eldar and G. Kutyniok, Eds. Cambridge, UK: Cambridge University Press, 2012.

[58] J. Richy, “Compressive Sensing in Medical Ultrasonography”, PhD thesis, KTH Royal Institute of Technology, Stockholm, Sweden (2012).

[59] N. Otsu, “A threshold selection method from gray-level histograms”, IEEE Transactions on Systems, Man, and Cybernetics 9.1 (1979): 62–66.

[60] https://www.mathworks.com/matlabcentral/fileexchange/41240-speckle-noise-reduction-in-ultrasound-images

[61] Y. Chen, R. Yin, P. Flynn, and S. Broschat, “Aggressive region growing for speckle reduction in ultrasound images”, Pattern Recognition Letters 24.4-5 (2003): 677–691.

[62] H. J Baskin, D. S Duick, R. A Levine, *Thyroid Ultrasound and Ultrasound-Guided FNA Biopsy.* MA: Kluwer Academic Publishers (2000): p.25.

[63] H. A. Akbar, “Efficient Similarity-Driven Emission Angle Selection for Coherent Plane-Wave Compounding”, MASc thesis, University of Victoria, Victoria, Canada (2018).

[64] A. Carovac, F. Smajlovic, and D. Junuzovic, “Application of ultrasound in medicine”, Acta Informatica Medica, 19.3 (2011):168–171.